Review Article

Nano Research
2023, 16(11): 12516–12530

ISSN 1998-0124 CN 11-5974/O4
https://doi.org/10.1007/s12274-023-6173-1

Pave the way to the batch production of SWNT arrays for carbon-based electronic devices

Ying Xie[1,§], Yue Li[2,§], Ziqiang Zhao[2], and Jin Zhang[1] (✉)

[1] *College of Chemistry and Molecular Engineering, Beijing Science and Engineering Center for Nanocarbons, Beijing National Laboratory for Molecular Sciences, Peking University, Beijing 100871, China*
[2] *State Key Laboratory of Nuclear Physics and Technology, School of Physics, Peking University, Beijing 100871, China*
[§] *Ying Xie and Yue Li contributed equally to this work.*

Received: 15 June 2023 / **Revised:** 7 September 2023 / **Accepted:** 7 September 2023

ABSTRACT

Single-walled carbon nanotubes (SWNTs) have been regarded as one of the most promising candidates to supplement or even replace silicon in the post-Moore era. The requirement is to prepare the horizontally aligned SWNTs arrays (HASAs) with multiple indicators, including high density, high semiconducting purity, and wafer-scale uniformity. However, after all the fevered works being done in controlled synthesis, we still have a long way to go before realizing the application of SWNTs in highly performed electronic devices. The methods of batch production and high-throughput characterization techniques of the HASAs are the two main challenges. In this outlook, we first summarized the progresses in synthesis of HASAs with either high density or high semiconducting purity. Then the methods adopted in characterizing SWNTs and HASAs were discussed according to the different principles of characterization techniques. Afterwards, the development of carbon nanotube based electronic devices, specifically, the field effect transistors (FETs), was reviewed from three perspectives. The problems involved in electronic applications bring forward the higher request to the HASAs itself. Therefore, in the end of this outlook, we prospected the future of the synthesis and corresponding characterization of HASAs, and tried to provide our ideas about how to pave the way to the batch production of HASAs for carbon based electronic devices.

KEYWORDS

horizontally aligned carbon nanotubes, batch production, high-throughput characterization, electronic application

1 Introduction

The increasing demand in improving the performance and energy efficiency of electronic devices and their scaling up has heightened the research heat for next-generation electronic systems based on new materials. Carbon nanotubes (CNTs) have been considered as one of the most promising materials because of their excellent electronic properties. As a one-dimensional nanomaterial, the carrier mobility of single-walled CNTs (SWNTs) can be as high as 100,000 cm^2/Vs. The CNT-based field effect transistors (FETs) show ideal ballistic transport characteristics [1, 2]. Compared with silicon-based metal-oxide-semiconductor (MOS) transistors, the current tolerance density, switching speed, switching ratio, and mobility of CNT-based FETs can be improved by several orders of magnitude. However, to achieve the cutting-edge applications, the controlled synthesis of SWNTs is still challenging.

Compared to other types of SWNTs, the horizontally aligned SWNT arrays (HASAs) are of particular interest, especially because of its suitability for the integrated circuits (ICs) with high performance. There are mainly two synthetic routes of HASAs, one is direct growth, and the other is post-treatment. Each has its advantages and disadvantages. It is too early to judge which method can finally pave the way to the batch production of HASAs for electronics. In this outlook, we mainly focused on the first one—the direct growth methods. It is generally accepted that chemical vapor deposition (CVD) is the most promising way of controlled synthesis of SWNTs. To assemble SWNTs into horizontal arrays during growth, different external forces have been exerted, such as electric field, gas flow, atomic step, and crystal lattice [3–6]. Among these mechanisms of aligning, HASAs grown on single crystal substrate tend to have a higher alignment, and the controllability of their structures and properties.

To be applied in cutting-edge fields such as carbon-based electronics, the HASAs are required with multiple indicators, including perfect alignment, high density, high semiconducting purity, and a wafer-scale uniformity [7]. Past few decades have witnessed inspiring progresses in controlled synthesis of HASAs with one or two excellent indicators that mentioned above. Nevertheless, many challenges arise when we try to combine these progresses and achieve batch production of HASAs for carbon-based electronics. Of particular interest and complexity are the synchronous realization of the multiple indicators and the more efficient characterization of HASAs. In this outlook, we first reviewed the recent progresses and challenges in the synthesis and characterization of HASAs. Then we also explored the development of CNT-based field-effect transistors (CNT-FETs), which is one of the most important applications of HASAs. Finally, we tried to prospect the future opportunities and challenges of HASAs from a unified perspective, trying to find a possible way paving to its industrialization.

Address correspondence to jinzhang@pku.edu.cn

2 Synthesis of HASAs

Since the discovery of SWNT, a considerable amount of researches pertaining to SWNT growth mechanisms have been conducted. The process of growing SWNTs involves the activation of catalyst, the nucleation, growth, and termination of SWNT. The catalyst activation is a precondition for nucleation of SWNT, and the active phase is dependent on the reactive atmosphere. The growing atmosphere usually contains necessary carbon sources (such as C_2H_4, CH_4, C_2H_5OH, etc.), reductive gases (such as H_2), and inert gases (such as Ar or N_2) [8]. After catalyst activation, the SWNT nucleation starts from nucleating a cap on the catalyst surface by the assembly of excess carbon atoms. In a typical vapor–liquid–solid (VLS) model, dissociated carbon atoms dissolve into the liquid catalyst nanoparticle continuously. When supersaturated, the graphitic carbon precipitates as "cap precursor", and subsequently converts into a solid phase SWNT through constructing the sidewall between the cap and catalyst particle [9, 10]. Apart from VLS mechanism, there is also a vapor–solid (VS) model. The carbon atoms do not dissolve into, but rest on and bond with the surface of non-metallic catalyst nanoparticles, then transform into an SWNT cap [11–13]. According to extensive transmission electron microscopy (TEM) characterization, the SWNT nucleation can be classified into tangential and perpendicular modes, depending on whether the diameter of the nucleated SWNTs is similar to or smaller than that of the connected catalyst particles [14–16]. After nucleating a stable SWNT cap, subsequent incorporation of new carbon atoms into the cap rim leads to the elongation of the SWNT. The termination occurs until the catalyst is deactivated by several complicated factors, such as Ostwald ripening [17], or an excessive carbon supply [15]. With the careful control of each step, SWNTs with controlled structures and properties can be synthesized to satisfy various requirements of applications.

2.1 High density of HASAs

For preparing HASAs, one of the most important indicators is the density of nanotubes aligned in the arrays. In order to be as high as possible, two main designing philosophies have been adopted. One is to manipulate the catalysts, which govern the growth of SWNTs directly. The other is to manipulate the as-grown SWNTs, which is to assemble random distributed SWNTs into organized arrays on target substrates.

2.1.1 Manipulate the catalysts

To obtain higher density of HASAs, it is intuitive that managing to increase the number of catalysts before each growth begins would be helpful. As shown in Fig. 1(a), after one optimized growth, segments of the as-grown SWNTs were selectively exposed to an oxygen plasma, creating lines of bare quartz for the following deposition of fresh catalysts to initiate a second CVD growth. The density of HASAs in this sequential approach was estimated to be 20–30 tubes/μm. But the improvement of density was limited, only increased by 2–3 times [18]. In fact, simply increasing the number of catalyst nanoparticles seems not enough.

To pursue a higher density of HASAs, managing to increase the number of active nanoparticles is necessary. A multicycle CVD method was schematized in Fig. 1(b). By stopping the carbon feedstock intermittently for a short period between each growth cycle, the catalysts had more chance to be reactivated to nucleate new SWNTs, so as to restart the growth step [19]. With the increased percentage of activated catalyst particles, the density of HASAs was about 20–40 tubes/μm on quartz. However, the repeating cycle was limited to four times at most, otherwise the density would decline due to the competition between the growing and etching reactions during this process. Similar principle has been proposed in the "periodic" method. By periodically switching the carbon feedstock on and off, a wider diameter range of catalysts was allowed to bring about the nucleation of SWNTs [20]. Besides, a method of patterning

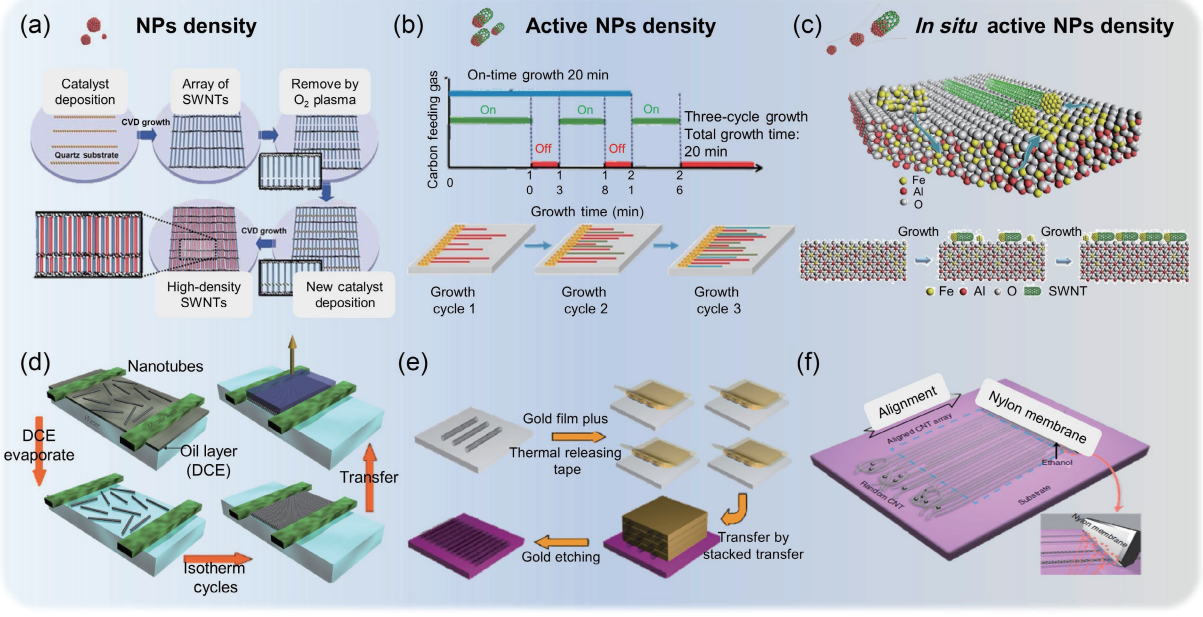

Figure 1 Synthesis of HASAs with high density by (a)–(c) manipulating the catalyst nanoparticles and (d)–(f) manipulating the SWNTs. (a) Schematic illustration of increasing the number of catalyst nanoparticles by sequential approach. Reproduced with permission from Ref. [18], © WILEY-VCH Verlag GmbH & Co. KGaA, Weinheim 2010. (b) Schematic illustration of increasing the number of active catalyst nanoparticles by three-cycle CVD growth. Reproduced with permission from Ref. [19], © American Chemical Society 2011. (c) Schematic illustration of increasing the number of active catalyst nanoparticles *in situ* by Trojan method. Reproduced with permission from Ref. [22], © Springer Nature Limited 2015. (d) Schematic illustration of Langmuir–Schaefer method. Reproduced with permission from Ref. [27], © Springer Nature Limited 2013. (e) Schematic illustration of stacked multiple transfer process. Reproduced with permission from Ref. [29], © Tsinghua University Press and Springer-Verlag Berlin Heidelberg 2010. (f) Schematic illustration of soft-lock drawing method. Reproduced with permission from Ref. [30], © Guo, Y. F. et al. 2022.

catalysts was used to avoid the merging of unreacted nanoparticles on substrate. With the improved number of active catalyst nanoparticles, the density of HASAs can be 50 tubes/μm [21]. Nevertheless, the density of HASAs obtained in the above-mentioned methods was still well below par. Because the number of nanoparticles that can be reactivated was limited, and might not be as active as fresh ones.

To maximize the catalyst utilization, a better solution would be to increase the number of active nanoparticles *in situ*. As shown in Fig. 1(c), the Trojan catalyst has been designed intelligently. The catalysts first dissolved and stored into the substrate during annealing, and then gradually released under H_2 reduction during growth. The reduced interaction between active catalysts led to less deactivation, thus increased the utilizing efficiency of catalysts obviously. The as-grown HASAs showed an ultra-high density of 130 tubes/μm [22]. Based on such an idea, Trojan–Mo catalyst [23] and magnesium-assisted catalyst anchoring strategy [24] have been proposed to further increase the local highest density and the distributing uniformity of HASAs, respectively. Besides, other ways of loading fresh catalysts continuously were also proved to be effective, such as from the growth atmosphere. For example, loading titanocene dichloride on spatially confined quartz substrate by floating catalyst CVD (FCCVD) [25] and multi-cycle loading fresh Cu on substrate through condensation of Cu vapor [26] can both grow HASAs with the density of 60–70 tubes/μm.

To sum up, the idea of manipulating catalysts to achieve high-density HASAs has undergone a transformation from simply increasing the number of catalyst nanoparticles, to increasing the active catalyst nanoparticles. And further, it is realized that increasing the number of active catalyst nanoparticles *in situ* should be much more promising, so as to meet the high-density requirement of applications.

2.1.2 *Manipulate the SWNTs*

Apart from manipulating catalyst nanoparticles before or during growing process, manipulating the as-grown SWNTs after growth has also been widely studied to increase the density of HASAs. For example, the large-area aligned SWNTs with an ultra-high density of more than 500 tubes/μm were assembled using the Langmuir–Schaefer method (Fig. 1(d)). The dispersed CNTs were first floated on the two-dimensional air/water interface during evaporation of the volatile organic solvent, then assembled into well-ordered arrays under a uniaxial compressive force applied by mobile barrier bars [27]. Besides liquid phase assembly, a stacked multiple transfer method has been developed. Gold films containing the aligned CNTs could be transferred layer-by-layer repeatedly, then etched away at the same time, so as to collapse the CNTs onto substrate (Fig. 1(e)). Repeating this process up to four times increased the density of HASAs to 55 tubes/μm [28, 29]. However, the relatively poor alignment and unwanted waviness of HASAs caused by any perturbation during such complex process might result in poor performance of CNT-based transistors. In order to simplify the manipulation, a soft-lock drawing method has been recently proposed to align random SWNT networks into high-density HASAs under the drawing force of the "soft" wetted nylon membrane (Fig. 1(f)). Such a method was free of any surfactant, non-destructive, and quite facile, opening up a new path for preparing HASAs with high density [30].

In a word, manipulating the SWNTs after growth tends to achieve a higher density of HASAs with large-area uniformity. However, compared with the substrate-oriented direct growth, the problems still remain in relatively poorer alignment of arrays, unavoidable contamination, degradation of quality, complex procedures of post-processing, and increased costs. These potential drawbacks might lead to scale-up problem during the application of these HASAs.

2.2 High semiconducting selectivity of HASAs

Obtaining SWNTs with specific conductivity, especially semiconducting, is another prerequisite for the cutting-edge applications. A great number of strategies have been proposed to attain this goal, which can be roughly divided into four specific implementation perspectives: design of the post-processing, the growth atmosphere, the catalysts, and a more fundamental guideline, the control of thermodynamics and kinetics.

2.2.1 *The design of post-processing*

A variety of post-processing methods have been developed to obtain SWNTs with uniform and specific electronic structure, such as the density gradient ultracentrifugation (DGU) [31], gel chromatography (GC) [32], aqueous two phases extraction (ATPE) [33], selective dispersion (SD) [34, 35], and so on. However, the high separation purity in these methods is often counteracted by the high technical threshold, the complexity of separating process and surfactants design, and the degraded quality of SWNTs. Therefore, these methods were not quite suitable for enriching specific SWNTs in HASAs. Alternatively, methods focused on post-processing the as-grown HASAs on the substrate have been proposed. As shown in Fig. 2(a), based on the different interactions of semiconducting and metallic SWNTs with different functional groups, a "Scotch tapes" strategy was created. By simply pressing and peeling off the polydimethylsiloxane thin film-supported tape either terminated with 3-aminopropyl-triethoxysilane (A-scotch tape) or triethoxyphenylsilane (P-scotch tape), the semiconducting or metallic SWNTs could be removed selectively, leaving approximately 90% metallic SWNTs or 85% semiconducting SWNTs on the substrate, respectively [36]. Likewise, metallic SWNTs could be "washed off" by a sodium dodecyl sulfate (SDS) aqueous solution, mainly leaving the semiconducting ones with the purity of 90% on the surface [37]. However, further improvement of the purity of SWNTs with specific conductivity without any contamination remains difficult in these separation techniques.

Under the guiding principle of the difference in the electronic structures between semiconducting and metallic SWNTs, the methods of preferentially destructing the slightly more reactive metallic SWNTs have been developed. For instance, selective oxidation could be induced by a current to electrically break down the metallic SWNTs [38]. Figure 2(b) showed an organic film-assisted electrical breakdown method: The HASAs were coated with organic films when applying voltage. The removal of full-length metallic SWNTs was promoted due to the propagation of exothermic oxidation of the organic film [39]. Alternatively, the selective oxidation of metallic SWNTs could also be conducted in a gas reaction. For example, exposing the SWNTs to CH_4 plasma [40] or light illumination [41] enhanced the semiconducting purity. However, the diameter of SWNT governs the chemical activity in these methods. The semiconducting SWNTs with relatively small diameters were also indiscriminately destructed. In order to avoid measurable destruction of semiconducting SWNTs, a method utilizing the nanoscale thermocapillary flow followed by etching has been proposed. As shown in Fig. 2(c), an ultrathin layer of thermocapillary resist was first deposited on HASAs on the substrate that patterned with metal and dielectric layers. When applying a suitable voltage, due to the unipolar p-type behavior of semiconducting SWNTs, the Joule heating would only occur in the metallic SWNTs region, which raised the temperature locally. Thus, trenches centered on the metallic SWNTs were produced. In the following ion etching, the exposed metallic SWNTs could be eliminated, leaving purified semiconducting HASAs on the substrate [42]. To simplify the tedious procedures of making electrodes and gating structures in the above method, the

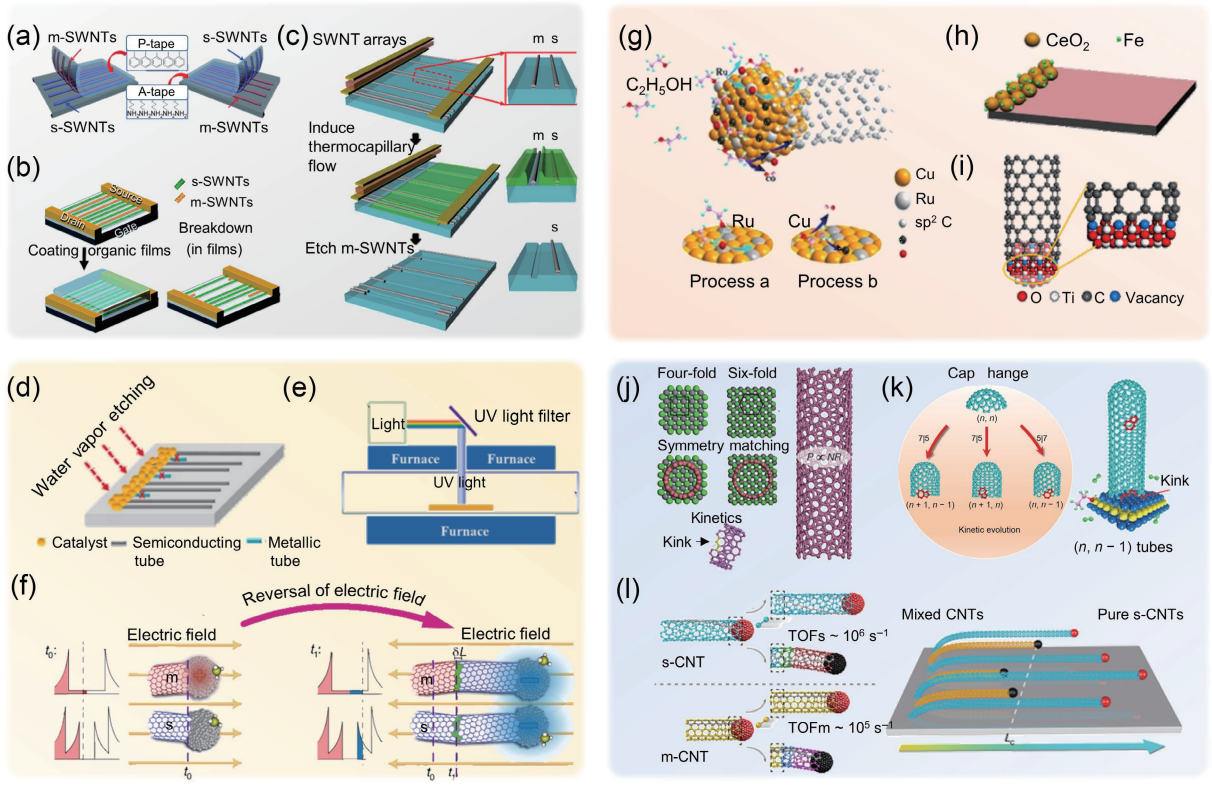

Figure 2 Synthesis of HASAs with high semiconducting purity by the design of (a)–(c) post processing, (d)–(f) growth atmosphere, (g)–(i) catalyst, and (j)–(l) the control of thermodynamics and kinetics. (a) Schematic illustration of "Scotch tapes" strategy to remove metallic or semiconducting SWNTs from substrate selectively. Reproduced with permission from Ref. [36], © Wiley-VCH Verlag GmbH & Co. KGaA, Weinheim 2011. (b) Schematic illustration of the organic film-assisted electrical breakdown method. Reproduced with permission from Ref. [39], © The Royal Society of Chemistry 2014. (c) Schematic illustration of inducing thermocapillary flow followed by etching. Reproduced with permission from Ref. [42], © Springer Nature Limited 2013. (d) Schematic illustration of the water etching method and the three important etching rules. Reproduced with permission from Ref. [51], © American Chemical Society 2012. (e) Schematic illustration of ultraviolet beam illumination method. Reproduced with permission from Ref. [53], © American Chemical Society 2009. (f) Schematic illustration of electro-renucleation approach. Reproduced with permission from Ref. [54], © Wang, J. T. et al. 2018. (g) Schematic illustration of a bimetallic CuRu catalyst. Reproduced with permission from Ref. [55], © American Chemical Society 2015. (h) Schematic illustration of a CeO_2 supported Fe catalyst. Reproduced with permission from Ref. [56], © American Chemical Society 2014. (i) Schematic illustration of an oxygen-deficient TiO_2 catalyst. Reproduced with permission from Ref. [58], © American Chemical Society 2014. (j) Growth of SWNTs with selective chirality by controlling the thermodynamic and kinetic. Reproduced with permission from Ref. [61], © Macmillan Publishers Limited, part of Springer Nature 2017. (k) Mechanism of growing (n, n − 1) and (n, n − 2) SWNTs at near equilibrium conditions. Reproduced with permission from Ref. [62], © Elsevier Inc. 2019. (l) Schematic illustration of the rate-selected growth of semiconducting CNTs. Reproduced with permission from Ref. [63], © Zhu, Z. X. et al. 2019.

microwave radiation can be implemented to initiate the thermocapillary flows. The purity of semiconducting SWNTs can be as high as 99.9925% [43]. Nevertheless, extending the above-mentioned methods to process the highly dense HASAs was problematic, because the density of SWNTs would be limited by the trench widths. Besides, the contaminations or damages to the residual SWNTs were inevitable during the complex purification process. Therefore, many *in situ* methods of selectively enriching semiconducting SWNTs have been deeply explored.

2.2.2 *The design of growth atmosphere*

Direct growing HASAs by CVD involved at least a suitable growth atmosphere and active catalysts, which are also the two breakthrough points of enhancing the percentage of semiconducting SWNTs during growth. In the growth atmosphere, the carbon feedstock can be carefully selected to facilitate the prioritized growth of semiconducting SWNTs, such as using isopropyl alcohol [44], ethanol-methanol mixture [45, 46], ethanol-methane mixture [47], and so on. One designing idea in common in these methods is relying on the preferential etching effect of metallic SWNTs by etchants produced by specific carbon feedstock during growth, such as radicals, H_2O, etc. [48, 49]. Such etching agents could also be introduced directly into growth atmosphere with subtle control of their amounts to enrich semiconducting SWNTs. H_2O, as an appropriate etchant, was used to treat SWNTs after growth. Typically, in the temperature range of 700–750 °C, introducing water vapor with a concentration of 2000–6000 ppm for 20–30 min was sufficient to eliminate most metallic SWNTs [50]. In Fig. 2(d), three important rules governed in water etching method of achieving a high semiconducting selectivity of SWNTs were summarized: First, a suitable H_2O concentration is required to ensure a proper etching rate of metallic SWNTs over semiconducting ones. Second, the H_2O vapor concentration needs to be lower than a critical value to maintain the growth of SWNTs. Third, a low carbon feeding rate is also necessary to ensure a lower growth rate than the etching rate of metallic SWNTs [51]. In addition to introduce special carbon sources or specific etchants, enriching semiconducting SWNTs during growth could be realized by utilizing external field as well. Similar to exposing SWNTs to CH_4 plasma after growth, a plasma enhanced CVD was demonstrated to preferentially grow semiconducting CNTs with a high purity of approximately 90% [52]. Likewise, the light-radiation induced selectivity could also be conducted *in situ* by introducing ultraviolet (UV) beam from a hole on the top of the furnace into the CVD system during growth (Fig. 2(e)). In a free radical reaction, the metallic SWNT caps were easily destroyed in the beginning of SWNT growth, leaving semiconducting HASAs with a high percentage of 95% [53].

Although the semiconducting purity of the as-grown SWNTs can be 90%–97%, most of the above-mentioned approaches were

resorted to the preferential etching principle of the more reactive metallic SWNTs, which was inevitably at the cost of the decreased density of HASAs. Therefore, designing a method based on a concept much closer to the intrinsic difference between metallic and semiconducting SWNTs is necessitated. As shown in Fig. 2(f), an electro-renucleation (ERN) approach has recently been proposed. After random nucleation of SWNTs, an electric field was first exerted to positively charge the Fe particles and most of the metallic SWNTs, while the semiconducting SWNTs would remain almost neutral because of their bandgaps. Then the polarity of the electric field was reversed, and the catalysts were negatively charged. Because the electronic density of states (DOS) of semiconducting SWNTs were larger, the re-nucleation barrier was much lower for metallic SWNTs to twist into semiconducting ones. Due to this intrinsic electronic structure difference in semiconducting and metallic SWNTs, a 99.99% percentage of semiconducting SWNTs was obtained, which provided a new perspective of designing the growth atmosphere of HASAs [54].

2.2.3 *The design of catalyst*

Another essential factor involved in selective synthesis of semiconducting SWNTs is catalyst nanoparticles. Special component and structure of catalysts have been widely designed to enrich semiconducting SWNTs during growth. For instance, as shown in Fig. 2(g), using bimetallic catalyst, such as CuRu, the semiconducting selectivity of 91% was achieved with ethanol as carbon source. The predominance of semiconducting SWNTs was attributed to the synergistic effect of Cu and Ru on decomposing ethanol. During growth, the carbon source C_{ads} was generated on Cu catalyst through C–C bond breakage, while the etchant O_{ads} was produced on Ru catalyst by breaking C–O bonds. With appropriate ratio of Cu and Ru, the metallic SWNT caps were destructed and the selectivity of semiconducting SWNTs increased [55]. Apart from generating oxygen by carbon source, the lattice oxygen released from reducible oxide support could also be used to enrich semiconducting SWNTs. As shown in Fig. 2(h), owing to the close contact of Fe with CeO_2 support, the lattice oxygen released steadily by CeO_2 in reducing atmosphere during growth would eliminate metallic SWNTs effectively, leaving semiconducting SWNTs with a percentage of 97% [56]. Other reducible oxide was also used to serve as oxygen-releasing support to enrich semiconducting SWNTs, such as ZrO_2 [57]. However, still based on the selective etching effect, the density of HASAs in the above-mentioned approaches seemed quite unsatisfactory. Therefore, designing special catalysts to grow metallic or semiconducting SWNTs differentially based on their intrinsic differences would be much more desirable. As shown in Fig. 2(i), an oxygen deficient TiO_2 nanoparticle was prepared to grow semiconducting HASAs selectively with purity of 95%. The high selectivity was ascribed to the difference in the formation energy of semiconducting and metallic SWNTs on the oxygen deficient TiO_2 nanoparticles, which was lower for the former one [58]. Likewise, SiO_x nanoparticles with controlled diameter and oxygen content were also carefully prepared to enhance the semiconducting purity of SWNTs to 91% [59]. Apart from the catalyst components, the structure of catalyst has also been specially designed to realize a high semiconducting selectivity, such as an acorn-like structure of Co catalyst with partial carbon-coating. The inner Co nanoparticle served as active catalytic phase, while the outer carbon layer functioned as a preventing layer to inhibit the aggregation of Co catalysts. This special structure ensured a perpendicular growth mode of SWNTs and a high semiconducting selectivity of > 95% [60].

2.2.4 *The control of thermodynamics and kinetics*

Growth parameters, such as the atmosphere, catalysts, etc., interact with each other and work together to determine the structure of SWNTs. Thus, a guideline of controlling SWNTs structure has been advanced based on the nucleation thermodynamics and growth kinetics of SWNTs. As shown in Fig. 2(j), by controlling the symmetry of the metal carbide catalyst, the SWNTs with symmetry matched with that of the solid catalyst template showed lower formation energies, thus favored to nucleate preferentially. Besides, those SWNTs with the most kinks at the SWNT–catalyst interface had the highest growth rate. Consequently, the ($2n$, n) SWNTs were enriched via selective nucleation of the SWNTs symmetrically matched with the catalyst surface, such as (12, 6) SWNT on Mo_2C and (8, 4) SWNT on WC [61]. Furthermore, under near-equilibrium conditions, to stabilize the (n, n) caps during the nucleation stage, it is energetically preferable for the mutation of (n, n) to (n, $n - 1$) SWNTs by adding an adjacent pentagon–heptagon (5|7) pair (Fig. 2(k)). Therefore, the semiconducting families of (n, $n - 1$) SWNTs exhibited a higher population by carefully designing the solid catalyst and tuning the growth conditions [62]. Apart from thermodynamics, a spontaneous purification of semiconducting SWNTs based on a rate-selected strategy has recently been developed (Fig. 2(l)). Due to the interlock relation between the SWNT bandgap structure and the adsorption energy of C_2, the semiconducting SWNTs exhibited a growth rate approximately 10 times faster than their metallic counterparts (~ 80 and ~ 7 μm/s, respectively). Therefore, at a length of 154 mm during a natural growth, almost all the metallic SWNTs decayed, resulting in a 99.9999% purity of semiconducting SWNTs [63].

To sum up, from post-processing of the as-grown HASAs, to *in situ* enriching semiconducting SWNTs by the design of growth atmosphere and catalyst nanoparticles, the principle of selectively growing SWNTs with controlled structure has been continuously constructed and improved. However, for all the fevered works being done, we still have a way to go before preparing HASAs with high density, high structural consistency, and wafer-scale uniformity simultaneously, which will necessitate further breakthroughs in synthetic methods.

3 Characterization of HASAs

After years of iteration, significant progress has been made in synthesis of HASAs with high density and high semiconducting selectivity. As with most nanomaterials, the development of HASAs synthesis is inseparable from effective characterization. According to the characterizing principles, the characterization techniques for SWNTs and HASAs can be roughly divided into three categories: optical imaging/spectroscopy, scanning probe microscopy (SPM), and electron microscopy. On a micro level, we normally pay attention to the morphology and structure of an individual SWNT. With the development of HASAs synthesis, macro properties, such as density, alignment, and CNT pitch in HASAs have become attractive. In this section, we compared and discussed the characterization methods of HASAs from two dimensions: techniques (optical imaging/spectroscopy, scanning probe microscopy, and electron microscopy) and scale (micro scale and macro scale).

3.1 Optical imaging/spectroscopy

On the micro level, the characterization of morphology of SWNTs comes first. Due to the simple structure of equipment and the ease of operation, the optical imaging has been widely used in morphological characterization of various materials. However, the resolution of optical microscope is limited by the diffraction limit.

Even though the high efficiency, traditional optical imaging fails in the characterization of nano-scale SWNTs. To make SWNTs observable in optical imaging, a variety of coating processes have been developed [64–66]. Figure 3(a) showed the method of depositing seeded electroless Au nanoparticles onto SWNTs. The morphology of SWNTs was successfully visualized, which was ascribed to the coupled surface plasmon resonance absorption of the Au nanoparticles [66]. However, the coating processes were complex and mostly detrimental to subsequent characterization and device performance. To develop nondestructive methods of imaging SWNTs optically, a vapor-condensation-assisted technique was proposed. Water vapor was blown to the sample during optical characterization. As the vapor condensed at SWNTs preferentially, the morphology of SWNTs can be identified by H_2O droplets [67]. Another more efficient method was polarization-based microscopy. Because of the strong depolarization effect of SWNTs, the optical contrast can be greatly enhanced by polarization manipulation (Fig. 3(b)) [68].

The structure of SWNT is another focus during characterization, including the defect density, diameter, and chirality of SWNTs. Raman spectroscopy is a powerful technique in this respect. As shown in Fig. 3(c), the typical Raman spectra of an SWNT consisted of four characteristic features: radial breathing mode (RBM)-mode, D-mode, G-mode, and 2D-mode (G') [22]. The RBM features correspond to the coherent vibration of the carbon atoms in the radial direction. There is a linear relationship between the position of RBM peak and the diameter of SWNT. By considering the Kataura plot (Fig. 3(d)), the chirality of SWNTs can be distinguished [69]. The D peak at ~ 1350 cm^{-1} is related to the disordering in SWNT lattice. In general, the more impurities and defects, the stronger the D peak. One can use the value of I_D/I_G to evaluate the defect density of the as-prepared SWNTs. Besides, the Rayleigh scattering spectra were also used to identify the excitation states in both semiconducting and metallic SWNTs [70]. Even a true-color image of SWNTs with diverse chiral indices can be acquired by the Rayleigh scattering microscope by immersing SWNTs in H_2O to enhance the Rayleigh scattering [71]. In addition, the spectrofluorimetric measurement was also used to characterize the structure of SWNTs. The density of electronic states of a single CNT was showed schematically in Fig. 3(e), where the values of E_{11} and E_{22} varied with the tube structure. Combing the fluorometric results with resonance Raman data, the diameter and chirality of SWNT can be identified rapidly [72]. However, the spectrum was susceptible to the interaction between SWNTs and substrates, so a complex isolation process of detaching SWNTs from substrates was necessary in this approach. As discussed above, polarization-based optical imaging can greatly enhance the contrast of SWNTs. Based on polarization optical system, the metallic/semiconducting SWNTs can be recognized from their color-resolved contrast in the optical image (Fig. 3(f)) [73]. Although the high-throughput feature of this method was quite charming, it required SWNTs with consistent diameter,

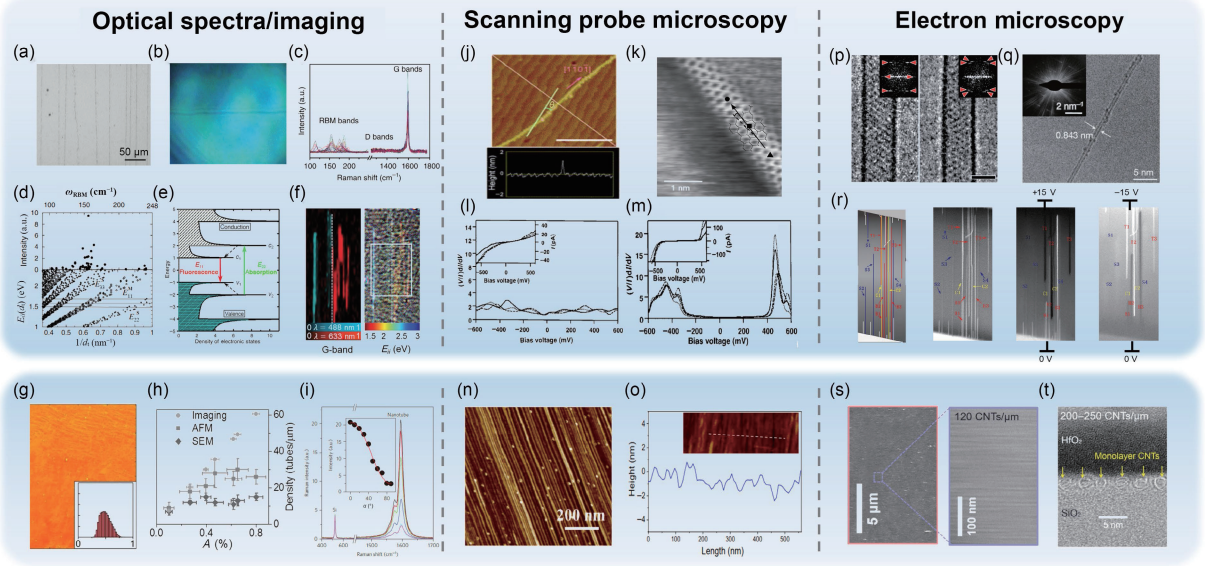

Figure 3 Characterization of HASAs by (a)–(i) optical imaging/spectroscopy, (j)–(o) scanning probe microscopy, and (p)–(t) electron microscopy. (a) Optical imaging of ultralong SWNTs by depositing Au nanoparticles. Reproduced with permission from Ref. [66], © Elsevier Ltd. 2010. (b) Optical imaging of SWNTs by polarization-based microscopy. Reproduced with permission from Ref. [68], © Springer Nature Limited 2013. (c) The typical Raman spectra of SWNTs. Reproduced with permission from Ref. [22], © Springer Nature Limited 2015. (d) The intensity and frequency of the RBM peaks vs. calculated gap energies as a function of the SWNTs diameter (later known as Kataura plot). Reproduced with permission from Ref. [69], © American Physical Society 2001. (e) Schematic of the density of electronic states for a single nanotube structure. Reproduced with permission from Ref. [72], © American Association for the Advancement of Science 2002. (f) Raman and optical imaging of a heterotube. Reproduced with permission from Ref. [73], © WILEY-VCH Verlag GmbH & Co. KGaA, Weinheim 2016. (g) Raman spectroscopy mapping of HASAs relative density; histogram of HASAs density is included as an inset. Reproduced with permission from Ref. [74], © Jinkins, K. R. et al. 2021. (h) Comparison between optical imaging, SEM, and AFM in determining the HASAs density. Reproduced with permission from Ref. [73], © WILEY-VCH Verlag GmbH & Co. KGaA, Weinheim 2016. (i) Alignment measurement of HASAs by polarized Raman spectra. Inset shows the dependence of the Raman intensity at 1594 cm^{-1} on angle. The red solid line is a fitting to $\cos^2(\alpha)$. Reproduced with permission from Ref. [27], © Springer Nature Limited 2013. (j) AFM image of SWNT grown on R-face sapphire substrate and the corresponding cross-sectional height profile (lower panel). Reproduced with permission from Ref. [6], © Elsevier B.V. 2005. (k) Atomic structure of an individual SWNT measured by STM. Calculated normalized conductance and measured I–V (inset) data (l) from a metallic SWNT and (m) from a semiconducting SWNT. Reproduced with permission from Ref. [77], © Macmillan Magazines Ltd. 1998. (n) Typical AFM image of direct-grown HASAs. Reproduced with permission from Ref. [23], © Tsinghua University Press and Springer-Verlag Berlin Heidelberg 2015. (o) AFM image (inset) and corresponding height profile of post-processed HASAs. Reproduced with permission from Ref. [76], © Liu, L. J. et al. 2020. (p) Typical TEM images of SWNTs and the FFT patterns (insets). Reproduced with permission from Ref. [78], © American Chemical Society 2008. (q) Diameter and chirality assignment of SWNT by TEM measurement and the corresponding ED pattern (inset). Reproduced with permission from Ref. [61], © Macmillan Publishers Limited, part of Springer Nature 2017. (r) Direct identification of metallic and semiconducting SWNTs by voltage contrast SEM measurement. Reproduced with permission from Ref. [79], © American Chemical Society 2012. (s) Density estimation of HASAs by SEM. (t) Density estimation and pitch uniformity measurement by TEM. Reproduced with permission from Ref. [76], © Liu, L. J. et al. 2020.

which is still difficult to achieve by direct growth of SWNTs at present.

On the macro level, the density, alignment, and pitch of SWNTs in arrays are "the three musketeers". In principle, the Raman intensity of the G-band is directly related to the density of HASAs. Therefore, the density distribution of HASAs can be measured by Raman mapping as shown in Fig. 3(g) [74]. Similarly, the optical reflection contrast is related to the absorption of SWNTs, so the density can be sequentially deduced from the integral optical absorption (Fig. 3(h)) [73]. However, both Raman intensity and optical contrast are influenced by multiple factors, including focusing, nature of substrates, impurities, and so on. Unless these non-negligible factors are decoupled, practical applications of these techniques remain challengeable.

Alignment is one of the most essential advantages of HASAs, which can be characterized semi-quantitatively by polarized Raman spectra [27, 75, 76]. Theoretically, CNTs with their tube axes parallel to the polarization direction of the incident laser are more likely to be excited. As shown in Fig. 3(i), the polarized Raman spectra were measured through rotating the polarizer. The alignment can be subsequently calculated from the maximum and minimum Raman intensity. The uniform pitch of SWNTs is necessary for electrical applications as well. However, as far as we know, no effective solution to characterize the pitch based on optical characterization has been demonstrated yet, probably due to the diffraction limit.

3.2 Scanning probe microscopy

Scanning probe microscopy is a range of microscopy developed for characterizing sample surface using a physical probe, including atomic force microscopy (AFM), electrostatic force microscopy (EFM), Kelvin probe force microscopy (KPFM), scanning tunneling microscopy (STM), and so on. Multiple information can be extracted from the interactions between the probe and surface. In the respect of CNTs, AFM and STM are the two most commonly used techniques.

On the micro level, the morphology of CNTs, substrates, and catalysts can be intuitively characterized by AFM. As shown in Fig. 3(j), the diameter of an SWNT and the angle between the SWNT and the steps of substrate can be obtained from one AFM image [6]. Furthermore, the diameter and distribution of catalysts, which influenced the diameter and density of SWNTs, can be distinguished by AFM as well. Therefore, AFM is a powerful technique for revealing the mechanism of the growth and alignment of HASAs.

As the first kind of SPM, STM senses the surface by an extremely sharp conducting tip, which can distinguish features smaller than 0.1 nm with a 0.01 nm depth resolution. With the high resolution, the atomic structure and electronic properties of SWNT can be obtained as shown in Figs. 3(k)–3(m). Specifically, the SWNT in Fig. 3(l) was metallic as the normalized conductance $(V/I)\mathrm{d}I/\mathrm{d}V$ stayed constant. The SWNT in Fig. 3(m) was semiconducting with a band gap of 750 mV, obtained from the sharp increase of $(V/I)\mathrm{d}I/\mathrm{d}V$ at −325 and +435 mV [77]. Although STM is very powerful on the micro level due to the principle of quantum tunneling, it requires conductive substrates and the measurement is time-consuming.

On the macro level, AFM is suitable for evaluating all the "three musketeers" of HASAs. The density per micrometers can be counted directly from an AFM image (Figs. 3(n) and 3(o)) [23]. Through appropriate data processing, statistical distribution of alignment and pitch of SWNTs can also be obtained. However, there remains two major problems in a wider range of applications of AFM: (1) the lack of benchmarking guidelines. For example, different researchers evaluated the density of HASAs under various scale bars, which made it difficult to compare the results from different reports. (2) Measurement efficiency is quite low. In order to obtain a high enough resolution of HASAs, the scan range is normally smaller than 5 μm. As the size of synthesized HASAs has already reached centimeter scale, AFM seems too cumbersome to reach a statistical significance.

3.3 Electron microscopy

Electron microscopy is a microscopic characterization method that uses a beam of accelerated electrons as the source of illumination. It mainly includes the transmission electron microscopy (TEM) and scanning electron microscopy (SEM). As the wavelength of an electron can be 100,000 times shorter than that of visible light, electron microscopes can reach atomic scale resolution.

High-resolution TEM (HRTEM) is a powerful technique to image the carbon atomic structure, thus the detailed structural information of an SWNT can be obtained [61, 78]. As shown in Figs. 3(p) and 3(q), the diameter and chirality of SWNT can be obtained from the TEM images with the fast Fourier transformation (FFT) patterns and the corresponding electron diffraction (ED) patterns. For example, the SWNT in Fig. 3(q) can be assigned to (8, 4) according to its ED pattern. Besides, one can also analyze the relationship between SWNTs and catalysts from TEM images, which are widely used in deducing the growth mechanism and modulating the structure of catalysts [61]. However, like STM, the processes of sample preparation and characterization are complex and time-consuming. Due to the simple and fast operation, SEM is more commonly used to characterize the morphology of SWNTs. More interestingly, as shown in Fig. 3(r), by applying different voltages between the upper and lower electrodes, SEM can also be used to distinguish metallic and semiconducting SWNTs from their different contrasts. Because of the good conductivity, metallic SWNTs could conduct more electrons from electrodes to the positively charged insulator surface, resulting in a higher voltage contrast in SEM than their semiconducting counterparts. However, the contrast is a relative measure, hence, the main challenge of this technique is how to establish a standard to identify individual SWNT quantitatively in practical applications [79].

In principle, the density, alignment, and pitch of HASAs can all be obtained from one SEM image. However, due to the discharge effect, the obtained lateral diameter will be broadened inevitably and the adjacent CNTs will become indistinguishable when the line density exceeds certain threshold. While in Fig. 3(s), by coating the SWNTs with an atomic layer deposition (ALD)-grown HfO_2, the contrast of SWNTs can be brighter, thus achieving better resolution. In addition, the density of HASAs can also be estimated roughly from TEM image, according to the spacings of SWNTs (Fig. 3(t)) [76]. However, the reliability of concluding that the entire HASAs have such a density counted from one TEM image is strongly determined by the uniformity of HASAs, which remains a big challenge in the respect of HASAs synthesis.

To sum up, great progresses have been made in characterization of SWNTs and HASAs, especially on microscale. One can obtain comprehensive information of an SWNT by making a reasonable selection from various techniques. However, the characterization of HASAs remains multiple challenges, such as the trade-off between the high throughput and high resolution, the lack of measurement standard and effective data processing method, and so on. Due to the rapid development of synthesis, effective evaluation of large-sized HASAs is highly demanded, which has become the road we must take before realizing the batch production and broader application of HASAs.

4 Electronic application of HASAs

Due to the outstanding electronic properties, SWNTs have been considered as one of the most promising materials for the next-generation electronics, especially for the field-effect transistors [80, 81]. In this section, we take the CNT-FETs as a representative to discuss the development of CNT-based electronic devices, and the requirements of HASAs.

Because of the perfect one-dimensional structure, there is almost no scattering during carrier transportation. Therefore, SWNTs have ultrahigh carrier mobility and ultralong mean free path, which ensures fast transient response and low power consumption of CNT-FETs. In addition, the diameter of SWNTs is about 1–2 nm, which may reduce short channel effects (SCEs) of CNT-FETs. As shown in Fig. 4, from the first CNT-FETs, to the 5 nm CNT-FETs that reach the quantum limit, further to the fabrication of three-dimensional (3D) ICs and wafer-scale electronics based on CNTs, studies on CNT-FETs continue to make breakthroughs. The study of CNT-FETs relied on the development of HASAs, and in return set new guidelines for the research of HASAs. The development of CNT-FET devices can be viewed from three perspectives: prototypes fabrication, process optimization, and performance exploration.

4.1 Prototypes of CNT-FET devices

As shown in Fig. 5(a), the first room-temperature CNT-FET was demonstrated in 1998 [82, 83]. However, the performance was far inferior to that of the silicon-based transistors of the same period. The problem mainly caused by the high contact resistance of the Pt electrode and the CNTs. The CNT-FET is basically operated as a Schottky barrier transistor. In order to reflect the inherent advantages of CNTs, contact electrode needs to be redesigned to reduce or eliminate the Schottky barriers between the CNTs and the metals. The work function of metal and wettability between metal and CNTs are the key factors.

In 2003, the first ballistic CNT-FET was fabricated. A high-work-function metal Pd was chosen as source-drain electrodes, realizing an Ohmic contact with semiconducting p-type CNTs [84]. As shown in Figs. 5(b) and 5(c), the "ON" state of semiconducting CNTs behaved like ohmically contacted ballistic metallic tubes, exhibiting room-temperature conductance near the ballistic transport limit of $4e^2/h$. Furthermore, through *in situ* modification of the electrode work function by hydrogen, the Schottky barrier of Pd and CNT contact was found to be zero or slightly negative (Fig. 5(d)).

As for n-type CNT-FETs, using metals with low-work-function is supposed to reduce the Schottky barriers. However, these metals are normally reactive and easily oxidized, leading to the rise of work function. Thus, besides work function and wettability, stability in air also needs to be considered. Until 2007, the metal Sc was used to afford ideal Ohmic contact with the conduction band of SWNTs [85]. As shown in Fig. 5(e), the as-fabricated CNT-FETs device was n-type, exhibiting "ON" state at large gate-source voltage (V_{gs}, ~ 10 V) and a near ballistic "ON" state conductance $G_{on} = 0.49G_0$ ($G_0 = 4e^2/h$) at 250 K.

So far, by mainly solving the contact problem between the electrode and CNTs, prototypes of both p-type and n-type CNT-FETs have been realized successively.

4.2 Optimization of CNT-FET devices

Beyond prototypes, researchers have made great efforts on optimizing CNT-FET devices to improve their performance. Device performance is evaluated by multiple indicators, corresponding to three main research focuses: electrodes contact, gate optimization, and integrated process.

CNTs have much higher carrier mobility than other semiconducting materials. In order to take advantage of this property, the first and the biggest challenge is how to obtain a good contact between electrodes and CNTs. As mentioned above, Ohmic contact has been achieved by choosing suitable metals. However, the size of these prototypes was only limited in microscale. When it comes to nanoscale, contact resistance rises dramatically [86, 87]. The most direct solution to reduce contact resistance is to use several parallel CNTs as a channel for each FET, which sets a higher request to the density of HASAs. According to the international roadmap for devices and systems community by IEEE, the density needs to be 270–410 tubes/μm. The current synthetic methods of HASAs are still far away from this target. Another route is to reduce the contact resistance of an individual CNT. In 2015, researchers proposed a solution by forming chemical bonds between CNTs and electrode, named as "end-bonded contacts". Through annealing treatment, metal electrodes reacted with CNTs and formed metal carbide (Fig. 5(f)). Contact resistance was remarkably down to 25–35 kΩ/tube. Moreover, for end-bonded contacts, the resistance was independent of contact size scaling from 300 to 20 nm as shown

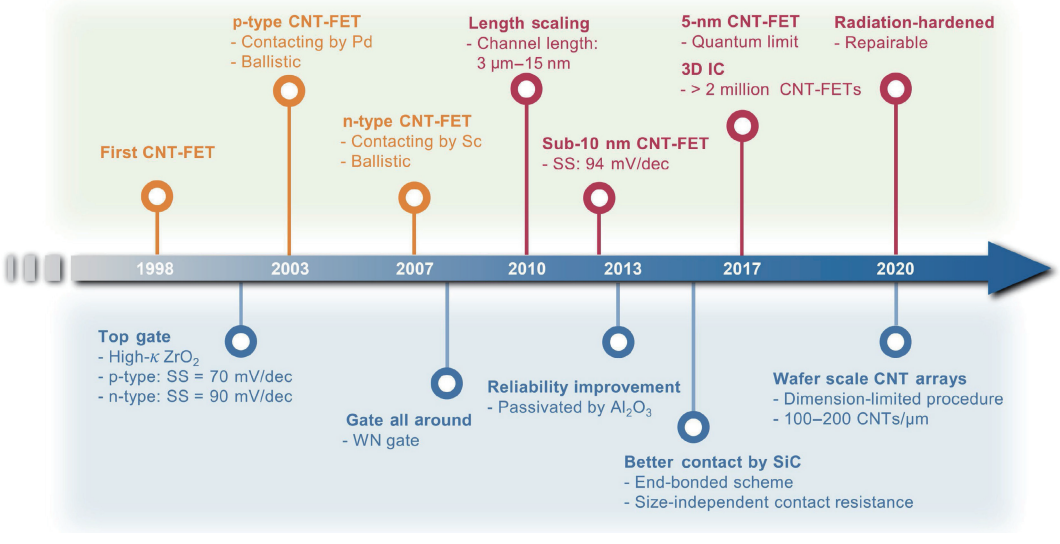

Figure 4 Development history of CNT-FET devices. The three perspectives: prototypes fabrication, process optimization, and performance exploration are shown in orange, blue, and red fonts, respectively.

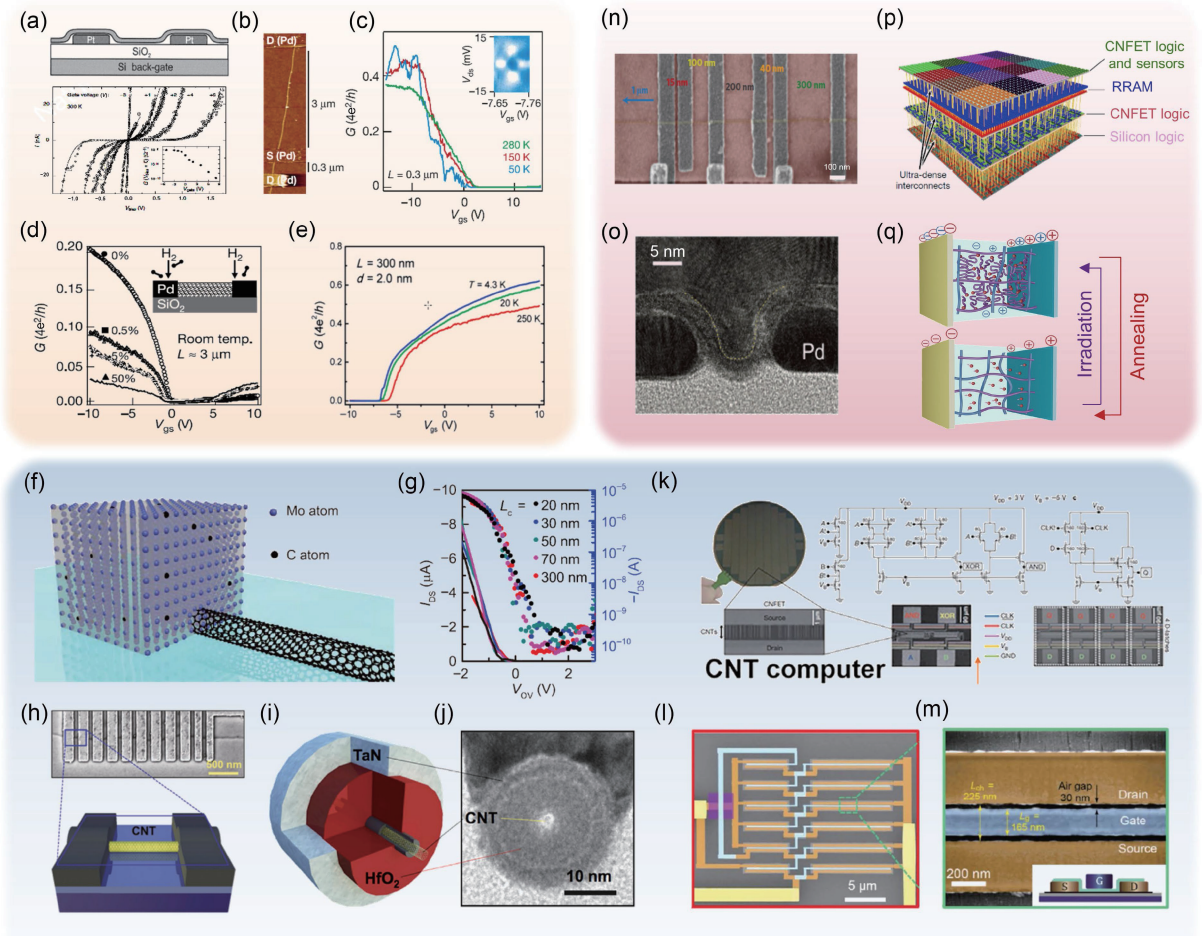

Figure 5 Electronic applications of HASAs focusing on FETs. (a)–(e) Prototypes of CNT-FET devices, (f)–(m) optimization of CNT-FET devices, and (n)–(q) performance exploration of CNT-FET devices. (a) Schematic illustration of the first room-temperature CNT-FET and the corresponding two-prove I–V_{bias} curves for various of the gate voltage (lower panel). Reproduced with permission from Ref. [82], © Macmillan Magazines Ltd. 1998. (b) AFM image of a representative ballistic p-type CNT-FET device. (c) Low bias conductance G versus V_{gs} for a 300-nm-long tube section on the same tube as for (b) at various temperatures. (d) Properties of the metal/semiconducting SWNT contacts as influenced by *in situ* metal work-function modification. Reproduced with permission from Ref. [84], © Macmillan Magazines Ltd. 2003. (e) Low bias conductance G versus V_{gs} for the first ballistic n-type back-gated CNT-FET device. Reproduced with permission from Ref. [85], © American Chemical Society 2007. (f) Schematic illustration of Mo end-contacted CNT-FET device. (g) Contact length scaling of Mo end-contacted CNT-FET device. Reproduced with permission from Ref. [1], © American Association for the Advancement of Science 2015. (h) SEM image and schematic illustration of the back-gated sub-10 nm CNT-FET device. Reproduced with permission from Ref. [92], © American Chemical Society 2012. (i) Schematic illustration of the gate-all-around CNT-FET device. (j) TEM cross-sectional imaging of the gate-all-around CNT-FET device. Reproduced with permission from Ref. [93], © American Chemical Society 2013. (k) CNT-FET subcomponents in a CNT computer. Reproduced with permission from Ref. [94], © Springer Nature Limited 2013. (l) False-colored SEM image of a ring oscillator based on CNT-FETs. (m) The gate structure of the CNT-FET used for constructing the ring oscillators in (l). Reproduced with permission from Ref. [76], © Liu, L. J. et al. 2020. (n) False-colored SEM image of a set of CNT-FETs on the same nanotube with channel length ranging from 15 nm to 1 μm. Reproduced with permission from Ref. [95], © Springer Nature Limited 2010. (o) TEM image of a normal Pd-contacted CNT-FET with gate length of 5 nm. Reproduced with permission from Ref. [96], © American Association for the Advancement of Science 2017. (p) Schematic illustration of a 3D integrated circuit, containing CNT-FET computation units. Reproduced with permission from Ref. [98], © Macmillan Publishers Limited, part of Springer Nature 2017. (q) Schematic illustration of heating-induced radiation repairing processes of ion gel CNT-FETs. Reproduced with permission from Ref. [99], © Zhu, M. G. et al. 2020.

in Fig. 5(g), and remained unchanged even for contact length below 10 nm. This method provided a new perspective to optimize the contacts.

The second research focus is the gate optimization, which determines the performance of switching. In 2002, the high-κ dielectrics, zirconium oxide, was designed as gate dielectrics through atomic layer deposition. The high capacitance of ZrO_2 dielectrics led to subthreshold swings (S) of ~ 60–80 mV per decade for p-type FETs and S ~ 90–100 mV per decade for n-type FETs [88]. The performance was further improved by using other high-k materials as gate insulators, such as HfO_2 and La_2O_3 films [89, 90]. Besides, the design of gate structure is another strategy to improve the efficiency of gate control. Basically, there are three kinds of geometry structures: back gate, top gate, and gate-all-around. From the fabricating point of view, back gate is the simplest structure for CNT-FETs. In 2012, a back-gated sub-10 nm CNT-FET was demonstrated to have a subthreshold swing of S ~ 94 mV per decade [91]. However, the presence of charge trapping in the vicinity of the nanotube channel caused hysteresis and threshold voltage variation. By employing a top-coated and hydrophobic monolayer to passivate bottom-gated devices (Fig. 5(h)), hysteresis and threshold voltage variation were reduced by average values of 84% and 53% [92]. Theoretically, top-gated CNT-FETs have higher gate control capability, but the performance of which is mainly limited by the deposition process as discussed above. Among the three gates, a gate-all-around structure is expected to be the most ideal geometry that maximizes the electrostatic gate controllability in FETs, but to be the most complex one for fabrication. As shown in Figs. 5(i) and 5(j) [93], Franklin's group reported CNT-FETs with self-aligned gates scaled down to 20 nm in the ideal gate-all-around geometry. Both p-type and n-type CNT-FETs were fabricated using Al_2O_3 and HfO_2 as dielectrics, respectively. This research provided an outstanding prototype for the ideal gate geometry. However, due

to the complexity of fabrication and the demanding for high alignment of HASAs, this structure has been yet only presented on an individual CNT.

The third research focus is the integrated process of CNT-FETs. In 2013, a research group demonstrated a systematically integrated process, which combined circuit design, growth, and transfer of CNTs, removal of metallic CNTs by electrical breakdown and device fabrication [94]. As shown in Fig. 5(k), the first CNT computer was fabricated from 178 FETs, each of which was composed of ~ 100–200 CNTs. Furthermore, the authors demonstrated the ability of this CNT-computer to run programs and a basic operating system that performed multitasking. In 2020, Peng's group presented another integrated process after years of researches [76]. The HASAs with high semiconducting-purity and high-density were first prepared on a 4-inch silicon wafer. Polymer residuals were removed by an yttrium oxide coating and decoating (YOCD) technique. Integrated top-gate FETs were then fabricated by a multiple process using electron-beam lithography (EBL) and ALD. Finally, the ring oscillator showing high performance was presented, as shown in Figs. 5(l) and 5(m). These breakthroughs of IC technology based on CNTs have shown great potential for future applications.

4.3 Performance exploration of CNT-FET devices

To explore the upper limit of CNT-FETs, researchers have made great efforts on further performance exploration on CNT-FETs. Scale reducing has been one of the most important strategies for the development of traditional silicon-based electronics in the past few decades. However, the problems of current leakage, energy loss, and heat production limit the further reducing of device scale. The one-dimensional nanoscale structure of CNTs makes it natural for sub-10 nm technology nodes. The scale of an individual FET consists of two critical lengths: the channel length (L_{ch}) and the contact length (L_c) [95]. In 2010, Franklin and Chen systematically studied the length scaling of CNT-FETs by fabricating CNT-FETs with different L_{ch} (3 μm–15 nm) or L_c (300–20 nm). Results showed that L_{ch} can be scaled down to 15 nm (Fig. 5(n)) without incurring short-channel effects. On the other hand, contact resistance was proved to be related to L_c, which means the performance cost of L_c scaling needs to be balanced for future fabrication of CNT-FETs. In 2012, they further reduced the L_c to 9 nm with Pd contacts and HfO_2 dielectric layer, making the FETs show an impressively small inverse subthreshold slope of ~ 94 mV per decade [91]. In 2017, top-gated CNT-FETs with a gate length of 5 nm were successfully fabricated (Fig. 5(o)) [96]. Graphene contacts were further used, leading to a slightly reduced on-state current but a substantially improved off-state performance. The subthreshold wing was ~ 73 mV per decade. It is worth noting that this 5 nm CNT-FET approached the quantum limit of FETs by using only one electron per switching operation.

Besides length scaling, 3D fabrication is another strategy to improve the integration level. In principle, the fabricating process of CNT-FETs is more suitable for 3D integration because of the lower temperature and the avoidance of complex procedures such as doping by ion implantation. In 2014, Shulaker et al. combined silicon-based FETs and CNT-FETs, and first realized monolithic 3D integration of logic and memory in arbitrary vertical stacking order [97]. Later in 2017, they further demonstrated a 3D chip [98], containing resistive random-access memory (RRAM) arrays, silicon and CNT-FET computation units, memory access circuitry, and more than one million carbon-nanotube field-effect transistors (CNFETs)-based gas sensors for inputs. All these were fabricated on overlapping vertical layers (Fig. 5(p)). This complex 3D electronics could sense and classify ambient gases.

Moreover, carbon-based electronics show potentials in some unique scenarios. For example, devices that operate in outer space and nuclear reactors require radiation-hardened transistors. The channel and gate of a traditional silicon-based FET are easily damaged by high-energy radiation. As shown in Fig. 5(q), a radiation-hardened FET has been reported, using semiconducting CNTs as the channel, an ion gel as the gate, and polyimide as the substrate [99]. CNTs have nanoscale cross-sections and low atomic number, which make them naturally radiation resistant. The as-prepared ICs showed a radiation tolerance up to 15 Mrad. More interestingly, the radiation damage was proved to be reparable through a simple annealing process at 100 °C. In addition, attractive attempts have been made in the low-temperature devices and flexible ICs [100–102]. The unique applications of CNT-based electronics are worthy of further exploration and research.

In a word, from the fabrication of prototypes, to the performance optimization and the exploration of CNT-FETs, remarkable progresses have been made in the past decades. However, CNT-FET research is still in the laboratory stage. In order to pave the way to practical applications, several problems need to be overcome, such as the improvement of contact resistance and reliability, the development of manufacturing compatible process, and more importantly, the further improvements of HASAs itself. The optimizations of CNT-FETs would benefit from, and in turn set higher requirements of the synthesis and characterization of HASAs. It requires preparing HASAs with wafer-scale uniformity, high density of 125 tubes/μm, high semiconducting purity of 99.9999%, consistent SWNT pitch and uniform diameter larger than 1.4 nm, as well as developing reliable characterization techniques of these properties.

5 Outlook

Based on the current progresses in synthesis and characterization of HASAs, the future lies in advancing the laboratory growth towards the industrialization. Firstly, realizing batch preparation of HASAs with all the required indicators, including a wafer-scale uniformity, high density, high semiconducting purity, and consistent pitch and diameter of SWNTs, is needed. Besides, developing a standardized characterization platform with both high throughput and high resolution is also highly required to evaluate the as-prepared HASAs thoroughly.

In order to prepare HASAs with all the required indicators, combining some of the effectual methods of synthesizing HASAs discussed in the previous section can be a choice. In recent years, diverse such combined methods to post-process SWNTs into arrays with not only high density but also semiconducting enrichment have been developed, such as the floating evaporation self-assembly (FESA) method [103], the modified slow vacuum filtration method [104], the liquid/liquid interface self-organization method [74], the directional shrinking method [105], the DNA brick crystal-based nanotrenches [106], and so on. However, it seemed all these methods were problematic in some way, such as the difficulty to scale up and the harsh conditions required to arrange SWNTs into ordered structures. Nevertheless, a recently proposed post-processing method was inspiring in realizing wafer-scale HASAs with both high density and semiconducting purity. Figures 6(a) and 6(b) schematically demonstrated the multiple dispersion and sorting method combined with a dimension-limited self-alignment (DLSA) process. The prepared HASAs showed well alignment (within alignment of 9 degrees), extremely high semiconducting purity (> 99.9999%), and tunable density of 100 to 200 tubes/μm on a 10-cm silicon wafer [76]. Nevertheless, when industrialization, the

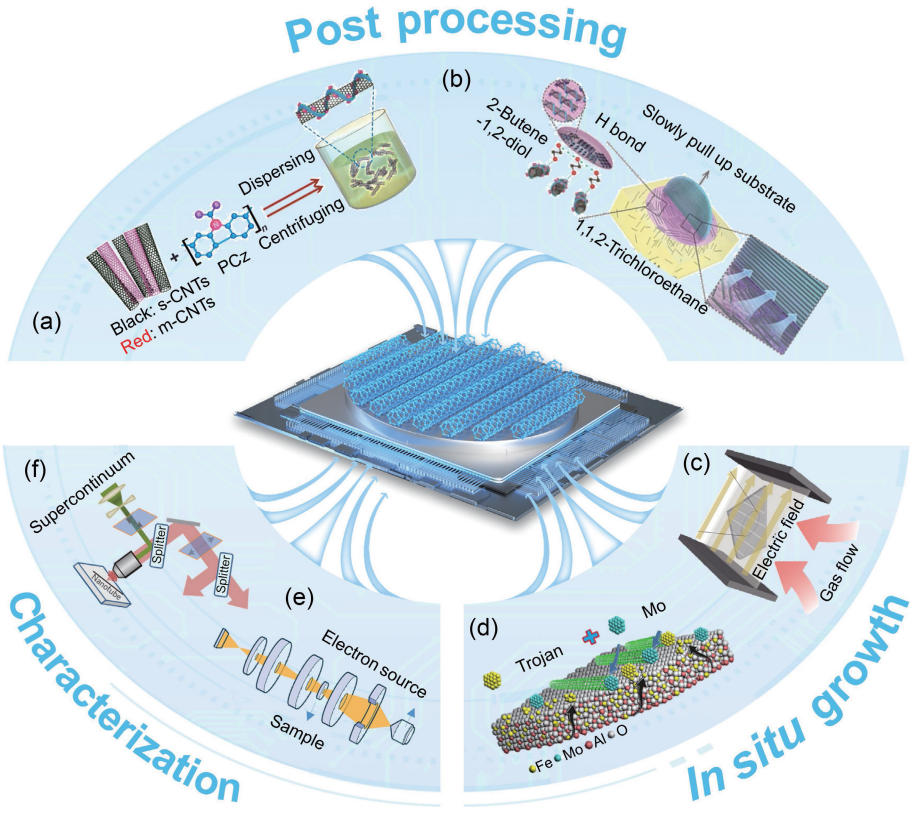

Figure 6 Outlooks for the synthesis and characterization of HASAs. (a) Schematic illustration of the multiple dispersion and sorting method to enrich semiconducting CNTs. (b) Schematic illustration of a DLSA process to obtain high-density HASAs. Reproduced with permission from Ref. [76], © Liu, L. J. et al. 2020. (c) The method of growing CNTs with the current highest semiconducting purity by the electro-renucleation approach. Reproduced with permission from Ref. [54], © Wang, J. T. et al. 2018. (d) The method of growing CNTs with the current highest density by the Trojan catalyst and its derived method. Reproduced with permission from Ref. [23], © Tsinghua University Press and Springer-Verlag Berlin Heidelberg 2015. (e) Schematic illustration of TEM, representing techniques with high resolution. (f) Schematic illustration of the polarization-based optical microscopy, representing techniques with high throughput. Reproduced with permission from Ref. [68], © Springer Nature Limited 2013.

relatively complicated process of most post-processing methods probably led to some potential problems of reproducibility, excessive costs, and possible damage to HASAs.

Direct growing HASAs with high density, semiconducting selectivity and wafer-scale uniformity simultaneously can be an alternative choice. For now, in methods of direct growth, the highest semiconducting purity of 99.9999% has been reported by electro-renucleation approach (Fig. 6(c)) [54], or spontaneous purification approach when reaching the CNT length of more than 154 mm [63]. The highest density of HASAs has been realized by Trojan and its derived catalyst system, such as 160 tubes/μm with Trojan–Mo catalyst (Fig. 6(d)) [23]. Although they both satisfied with one of the required indicators of HASAs respectively, a direct growth method of not only growing HASAs with all the required indicators, but also conducting in a facile way that is compatible with industrialization has not yet been established. With this goal in mind, we propose that the main growing parameters in direct growth of HASAs, such as the uniformity of substrate morphology, catalyst distribution, and gas flow, should be handled as a whole and optimized synchronously. Besides, integrating these separated processes in an assembly line is also highly desired. Another problem which continues to hinder the commercialization of CNT-based products and should never be ignored any more is the lack of consistency in the growing results. The growth of HASAs can be influenced by not only the growth parameters, but also the experiment-to-experiment variations, such as the growing carbon deposits on the reactor wall, variable ambient lab conditions including moisture and temperature, and so on. All of these unpredictable factors might overwhelm every attempt to optimize the growth parameters when trying to industrialize the preparation of HASAs. Therefore, it is highly recommended to establish a standardized recipe of preparing HASAs, from optimizing the growth parameters synchronously, to building an automatic CVD system that sets in a well-controlled lab environment.

Apart from synthesis, for the purpose of applying in high-end fields, one last gap needs to be filled in is the thorough, precise, and efficient evaluation of the as-prepared HASAs. Currently, progresses in characterization methods of SWNTs are mainly focused on being thorough and precise. In typical, techniques with high resolution can be used to obtain the most refined structure of SWNT, which provides valuable feedbacks in the stage of laboratory research of HASAs. For example, Fig. 6(e) schematically illustrated the structure of TEM, which is a representative of these thorough and precise characterization techniques. However, when towards industrialization, we will face a difficult scenario in effective evaluation of HASAs with relative macroscopic properties, such as the wafer-scale density, alignment, purity, and pitch. Normally, these macroscopic properties were estimated from a microscopic region, making them not reliable enough for practical applications. To reflect the real properties of HASAs, obtaining statistical data from the entire wafer can be more scientific. Therefore, a high-throughput characterization technique is highly demanded. In this case, the optical imaging can be promising. Figure 6(f) demonstrated the experimental set-up of the polarization-based optical microscopy. Not only the complete structure of a single SWNT, but also the density and semiconducting purity of HASAs can be roughly estimated by the polarized optical imaging with a rather high efficiency [68]. The further development of optical techniques should focus on the improvement of the characterizing accuracy and precision. In addition to the development of characterization techniques,

developing more statistical methods for data analysis, such as the artificial intelligence (AI) algorithm, is also desirable. In a word, the future of characterization lies in developing new methods of both characterization techniques and data analysis. And they should be able to evaluate the macroscopic properties of HASAs both thoroughly and efficiently.

Furthermore, as the technology matures, the process of characterization and the method of data analysis should be standardized as well. Nowadays, the differentiation of characterization methods adopted in different research groups makes their data not that comparable with each other. By contrast, in the field of making FETs, the guidelines for reporting and benchmarking key parameters and performance metrics of FETs have recently been proposed [107]. This effort can strongly improve the research efficiency in the future. In the respect of characterization, we believe a similar guideline to standardize the characterization process and data analysis is highly desirable as well.

All in all, as the research of silicon-based electronic devices has been struggling for years, the CNTs need to seize the opportunities to cope with the challenges. In order to stand out among other materials, great efforts should be made in the synthesis of HASAs with multiple indicators to fulfill the requirements of high-end applications, such as high density, high semiconducting purity, high alignment, uniform pitch, and so on. Besides, developing a thorough, precise, and high-throughput characterization platform might be the key to the advent of the new era of CNT research. It can be predicted that efficient characterization methods would encourage further improvement of the controlled synthesis of HASAs. In a word, developing a standardized recipe of synthesis and characterization, as well as a statistical method of data analysis would help to pave the way to the industrialization and the corresponding high-end applications of HASAs in the near future.

Acknowledgements

This work was financially supported by the Ministry of Science and Technology of China (Nos. 2022YFA1203302, 2022YFA1203304, and 2018YFA0703502), the National Natural Science Foundation of China (No. 52021006), the Strategic Priority Research Program of CAS (No. XDB36030100), and the Beijing National Laboratory for Molecular Sciences (No. BNLMS-CXTD-202001).

References

[1] Cao, Q.; Han, S. J.; Tersoff, J.; Franklin, A. D.; Zhu, Y.; Zhang, Z.; Tulevski, G. S.; Tang, J. S.; Haensch, W. End-bonded contacts for carbon nanotube transistors with low, size-independent resistance. *Science* **2015**, *350*, 68–72.

[2] Peng, L. M.; Zhang, Z. Y.; Qiu, C. G. Carbon nanotube digital electronics. *Nat. Electron.* **2019**, *2*, 499–505.

[3] Zhang, Y. G.; Chang, A.; Cao, J. E.; Wang, Q.; Kim, W.; Li, Y. M.; Morris, N.; Yenilmez, E.; Kong, J.; Dai, H. J. Electric-field-directed growth of aligned single-walled carbon nanotubes. *Appl. Phys. Lett.* **2001**, *79*, 3155–3157.

[4] Jin, Z.; Chu, H. B.; Wang, J. Y.; Hong, J. X.; Tan, W. C.; Li, Y. Ultralow feeding gas flow guiding growth of large-scale horizontally aligned single-walled carbon nanotube arrays. *Nano Lett.* **2007**, *7*, 2073–2079.

[5] Ismach, A.; Kantorovich, D.; Joselevich, E. Carbon nanotube graphoepitaxy: Highly oriented growth by faceted nanosteps. *J. Am. Chem. Soc.* **2005**, *127*, 11554–11555.

[6] Ago, H.; Nakamura, K.; Ikeda, K. I.; Uehara, N.; Ishigami, N.; Tsuji, M. Aligned growth of isolated single-walled carbon nanotubes programmed by atomic arrangement of substrate surface. *Chem. Phys. Lett.* **2005**, *408*, 433–438.

[7] Franklin, A. D. The road to carbon nanotube transistors. *Nature* **2013**, *498*, 443–444.

[8] He, M. S.; Wang, Y.; Zhang, X. Y.; Zhang, H.; Meng, Y. N.; Shang, D. H.; Xue, H.; Li, D.; Wu, Z. J. Stability of iron-containing nanoparticles for selectively growing single-walled carbon nanotubes. *Carbon* **2020**, *158*, 795–801.

[9] Page, A. J.; Ohta, Y.; Irle, S.; Morokuma, K. Mechanisms of single-walled carbon nanotube nucleation, growth, and healing determined using QM/MD methods. *Acc. Chem. Res.* **2010**, *43*, 1375–1385.

[10] Wang, X.; He, M. S.; Ding, F. Chirality-controlled synthesis of single-walled carbon nanotubes-from mechanistic studies toward experimental realization. *Mater. Today* **2018**, *21*, 845–860.

[11] Takagi, D.; Kobayashi, Y.; Homma, Y. Carbon nanotube growth from diamond. *J. Am. Chem. Soc.* **2009**, *131*, 6922–6923.

[12] Liu, B. L.; Ren, W. C.; Gao, L. B.; Li, S. S.; Pei, S. F.; Liu, C.; Jiang, C. B.; Cheng, H. M. Metal-catalyst-free growth of single-walled carbon nanotubes. *J. Am. Chem. Soc.* **2009**, *131*, 2082–2083.

[13] Chen, Y. B.; Zhang, J. Diameter controlled growth of single-walled carbon nanotubes from SiO_2 nanoparticles. *Carbon* **2011**, *49*, 3316–3324.

[14] Fiawoo, M. F. C.; Bonnot, A. M.; Amara, H.; Bichara, C.; Thibault-Pénisson, J.; Loiseau, A. Evidence of correlation between catalyst particles and the single-wall carbon nanotube diameter: A first step towards chirality control. *Phys. Rev. Lett.* **2012**, *108*, 195503.

[15] He, M. S.; Magnin, Y.; Amara, H.; Jiang, H.; Cui, H. Z.; Fossard, F.; Castan, A.; Kauppinen, E.; Loiseau, A.; Bichara, C. Linking growth mode to lengths of single-walled carbon nanotubes. *Carbon* **2017**, *113*, 231–236.

[16] He, M. S.; Magnin, Y.; Jiang, H.; Amara, H.; Kauppinen, E. I.; Loiseau, A.; Bichara, C. Growth modes and chiral selectivity of single-walled carbon nanotubes. *Nanoscale* **2018**, *10*, 6744–6750.

[17] Amama, P. B.; Pint, C. L.; McJilton, L.; Kim, S. M.; Stach, E. A.; Murray, P. T.; Hauge, R. H.; Maruyama, B. Role of water in super growth of single-walled carbon nanotube carpets. *Nano Lett.* **2009**, *9*, 44–49.

[18] Hong, S. W.; Banks, T.; Rogers, J. A. Improved density in aligned arrays of single-walled carbon nanotubes by sequential chemical vapor deposition on quartz. *Adv. Mater.* **2010**, *22*, 1826–1830.

[19] Zhou, W. W.; Ding, L.; Yang, S.; Liu, J. Synthesis of high-density, large-diameter, and aligned single-walled carbon nanotubes by multiple-cycle growth methods. *ACS Nano* **2011**, *5*, 3849–3857.

[20] Wu, B.; Geng, D. C.; Guo, Y. L.; Huang, L. P.; Chen, J. Y.; Xue, Y. Z.; Yu, G.; Liu, Y. Q.; Kajiura, H.; Li, Y. M. Ultrahigh density modulation of aligned single-walled carbon nanotube arrays. *Nano Res.* **2011**, *4*, 931–937.

[21] Ding, L.; Yuan, D. N.; Liu, J. Growth of high-density parallel arrays of long single-walled carbon nanotubes on quartz substrates. *J. Am. Chem. Soc.* **2008**, *130*, 5428–5429.

[22] Hu, Y.; Kang, L. X.; Zhao, Q. C.; Zhong, H.; Zhang, S. C.; Yang, L. W.; Wang, Z. Q.; Lin, J. J.; Li, Q. W.; Zhang, Z. Y. et al. Growth of high-density horizontally aligned SWNT arrays using Trojan catalysts. *Nat. Commun.* **2015**, *6*, 6099.

[23] Kang, L. X.; Hu, Y.; Zhong, H.; Si, J.; Zhang, S. C.; Zhao, Q. C.; Lin, J. J.; Li, Q. W.; Zhang, Z. Y.; Peng, L. M. et al. Large-area growth of ultra-high-density single-walled carbon nanotube arrays on sapphire surface. *Nano Res.* **2015**, *8*, 3694–3703.

[24] Xie, Y.; Qian, L.; Lin, D. W.; Yu, Y.; Wang, S. S.; Zhang, J. Growth of homogeneous high-density horizontal SWNT arrays on sapphire through a magnesium-assisted catalyst anchoring strategy. *Angew. Chem., Int. Ed.* **2021**, *60*, 9330–9333.

[25] Qian, L.; Shao, Q.; Yu, Y.; Liu, W. M.; Wang, S. S.; Gao, E. L.; Zhang, J. Spatially confined CVD growth of high-density semiconducting single-walled carbon nanotube horizontal arrays. *Adv. Funct. Mater.* **2022**, *32*, 2106643.

[26] Liu, W. M.; Zhang, S. C.; Qian, L.; Lin, D. W.; Zhang, J. Growth of high-density horizontal SWNT arrays using multi-cycle *in-situ* loading catalysts. *Carbon* **2020**, *157*, 164–168.

[27] Cao, Q.; Han, S. J.; Tulevski, G. S.; Zhu, Y.; Lu, D. D.; Haensch, W. Arrays of single-walled carbon nanotubes with full surface coverage for high-performance electronics. *Nat. Nanotechnol.* **2013**, *8*, 180–186.

[28] Shulaker, M. M.; Wei, H.; Patil, N.; Provine, J.; Chen, H. Y.; Wong, H. S. P.; Mitra, S. Linear increases in carbon nanotube density through multiple transfer technique. *Nano Lett.* **2011**, *11*, 1881–1886.

[29] Wang, C.; Ryu, K.; De Arco, L. G.; Badmaev, A.; Zhang, J. L.; Lin, X.; Che, Y. C.; Zhou, C. W. Synthesis and device applications of high-density aligned carbon nanotubes using low-pressure chemical vapor deposition and stacked multiple transfer. *Nano Res.* **2010**, *3*, 831–842.

[30] Guo, Y. F.; Shi, E. Z.; Zhu, J. D.; Shen, P. C.; Wang, J. T.; Lin, Y. X.; Mao, Y. W.; Deng, S. B.; Li, B. N.; Park, J. H. et al. Soft-lock drawing of super-aligned carbon nanotube bundles for nanometre electrical contacts. *Nat. Nanotechnol.* **2022**, *17*, 331–331.

[31] Arnold, M. S.; Green, A. A.; Hulvat, J. F.; Stupp, S. I.; Hersam, M. C. Sorting carbon nanotubes by electronic structure using density differentiation. *Nat. Nanotechnol.* **2006**, *1*, 60–65.

[32] Liu, H. P.; Nishide, D.; Tanaka, T.; Kataura, H. Large-scale single-chirality separation of single-wall carbon nanotubes by simple gel chromatography. *Nat. Commun.* **2011**, *2*, 309.

[33] Khripin, C. Y.; Fagan, J. A.; Zheng, M. Spontaneous partition of carbon nanotubes in polymer-modified aqueous phases. *J. Am. Chem. Soc.* **2013**, *135*, 6822–6825.

[34] Nish, A.; Hwang, J. Y.; Doig, J.; Nicholas, R. J. Highly selective dispersion of single-walled carbon nanotubes using aromatic polymers. *Nat. Nanotechnol.* **2007**, *2*, 640–646.

[35] Zheng, M.; Jagota, A.; Semke, E. D.; Diner, B. A.; Mclean, R. S.; Lustig, S. R.; Richardson, R. E.; Tassi, N. G. DNA-assisted dispersion and separation of carbon nanotubes. *Nat. Mater.* **2003**, *2*, 338–342.

[36] Hong, G.; Zhou, M.; Zhang, R. X.; Hou, S. M.; Choi, W.; Woo, Y. S.; Choi, J. Y.; Liu, Z. F.; Zhang, J. Separation of metallic and semiconducting single-walled carbon nanotube arrays by "Scotch tape". *Angew. Chem., Int. Ed.* **2011**, *50*, 6819–6823.

[37] Hu, Y.; Chen, Y. B.; Li, P.; Zhang, J. Sorting out semiconducting single-walled carbon nanotube arrays by washing off metallic tubes using SDS aqueous solution. *Small* **2013**, *9*, 1306–1311.

[38] Collins, P. G.; Arnold, M. S.; Avouris, P. Engineering carbon nanotubes and nanotube circuits using electrical breakdown. *Science* **2001**, *292*, 706–709.

[39] Otsuka, K.; Inoue, T.; Chiashi, S.; Maruyama, S. Selective removal of metallic single-walled carbon nanotubes in full length by organic film-assisted electrical breakdown. *Nanoscale* **2014**, *6*, 8831–8835.

[40] Zhang, G. Y.; Qi, P. F.; Wang, X. R.; Lu, Y. R.; Li, X. L.; Tu, R. Y.; Bangsaruntip, S.; Mann, D.; Zhang, L.; Dai, H. J. Selective etching of metallic carbon nanotubes by gas-phase reaction. *Science* **2006**, *314*, 974–977.

[41] Zhang, Y. Y.; Zhang, Y.; Xian, X. J.; Zhang, J.; Liu, Z. F. Sorting out semiconducting single-walled carbon nanotube arrays by preferential destruction of metallic tubes using xenon-lamp irradiation. *J. Phys. Chem. C.* **2008**, *112*, 3849–3856.

[42] Jin, S. H.; Dunham, S. N.; Song, J. Z.; Xie, X.; Kim, J. H.; Lu, C. F.; Islam, A.; Du, F.; Kim, J.; Felts, J. et al. Using nanoscale thermocapillary flows to create arrays of purely semiconducting single-walled carbon nanotubes. *Nat. Nanotechnol.* **2013**, *8*, 347–355.

[43] Xie, X.; Jin, S. H.; Wahab, M. A.; Islam, A. E.; Zhang, C. X.; Du, F.; Seabron, E.; Lu, T. J.; Dunham, S. N.; Cheong, H. I. et al. Microwave purification of large-area horizontally aligned arrays of single-walled carbon nanotubes. *Nat. Commun.* **2014**, *5*, 5332.

[44] Che, Y. C.; Wang, C.; Liu, J.; Liu, B. L.; Lin, X.; Parker, J.; Beasley, C.; Wong, H. S. P.; Zhou, C. W. Selective synthesis and device applications of semiconducting single-walled carbon nanotubes using isopropyl alcohol as feedstock. *ACS Nano* **2012**, *6*, 7454–7462.

[45] Ding, L.; Tselev, A.; Wang, J. Y.; Yuan, D. N.; Chu, H. B.; McNicholas, T. P.; Li, Y.; Liu, J. Selective growth of well-aligned semiconducting single-walled carbon nanotubes. *Nano Lett.* **2009**, *9*, 800–805.

[46] Ibrahim, I.; Kalbacova, J.; Engemaier, V.; Pang, J. B.; Rodriguez, R. D.; Grimm, D.; Gemming, T.; Zahn, D. R. T.; Schmidt, O. G.; Eckert, J. et al. Confirming the dual role of etchants during the enrichment of semiconducting single wall carbon nanotubes by chemical vapor deposition. *Chem. Mater.* **2015**, *27*, 5964–5973.

[47] Kang, L. X.; Zhang, S. C.; Li, Q. W.; Zhang, J. Growth of horizontal semiconducting SWNT arrays with density higher than 100 tubes/μm using ethanol/methane chemical vapor deposition. *J. Am. Chem. Soc.* **2016**, *138*, 6727–6730.

[48] Li, W. S.; Hou, P. X.; Liu, C.; Sun, D. M.; Yuan, J. T.; Zhao, S. Y.; Yin, L. C.; Cong, H. T.; Cheng, H. M. High-quality, highly concentrated semiconducting single-wall carbon nanotubes for use in field effect transistors and biosensors. *ACS Nano* **2013**, *7*, 6831–6839.

[49] Sakurai, S.; Yamada, M.; Sakurai, H.; Sekiguchi, A.; Futaba, D. N.; Hata, K. A phenomenological model for selective growth of semiconducting single-walled carbon nanotubes based on catalyst deactivation. *Nanoscale* **2016**, *8*, 1015–1023.

[50] Li, P.; Zhang, J. Sorting out semiconducting single-walled carbon nanotube arrays by preferential destruction of metallic tubes using water. *J. Mater. Chem.* **2011**, *21*, 11815–11821.

[51] Zhou, W. W.; Zhan, S. T.; Ding, L.; Liu, J. General rules for selective growth of enriched semiconducting single walled carbon nanotubes with water vapor as *in situ* etchant. *J. Am. Chem. Soc.* **2012**, *134*, 14019–14026.

[52] Li, Y. M.; Mann, D.; Rolandi, M.; Kim, W.; Ural, A.; Hung, S.; Javey, A.; Cao, J. E.; Wang, D. W.; Yenilmez, E. et al. Preferential growth of semiconducting single-walled carbon nanotubes by a plasma enhanced CVD method. *Nano Lett.* **2004**, *4*, 317–321.

[53] Hong, G.; Zhang, B.; Peng, B. H.; Zhang, J.; Choi, W. M.; Choi, J. Y.; Kim, J. M.; Liu, Z. F. Direct growth of semiconducting single-walled carbon nanotube array. *J. Am. Chem. Soc.* **2009**, *131*, 14642–14643.

[54] Wang, J. T.; Jin, X.; Liu, Z. B.; Yu, G.; Ji, Q. Q.; Wei, H. M.; Zhang, J.; Zhang, K.; Li, D. Q.; Yuan, Z. et al. Growing highly pure semiconducting carbon nanotubes by electrotwisting the helicity. *Nat. Catal.* **2018**, *1*, 326–331.

[55] Zhang, S. C.; Hu, Y.; Wu, J. X.; Liu, D.; Kang, L. X.; Zhao, Q. C.; Zhang, J. Selective scission of C–O and C–C bonds in ethanol using bimetal catalysts for the preferential growth of semiconducting SWNT arrays. *J. Am. Chem. Soc.* **2015**, *137*, 1012–1015.

[56] Qin, X. J.; Peng, F.; Yang, F.; He, X. H.; Huang, H. X.; Luo, D.; Yang, J.; Wang, S.; Liu, H. C.; Peng, L. M. et al. Growth of semiconducting single-walled carbon nanotubes by using ceria as catalyst supports. *Nano Lett.* **2014**, *14*, 512–517.

[57] Lin, D. W.; Yu, Y.; Li, L. Y.; Zou, M. Z.; Zhang, J. Growth of semiconducting single-walled carbon nanotubes array by precisely inhibiting metallic tubes using ZrO_2 nanoparticles. *Small* **2021**, *17*, 2006605.

[58] Kang, L. X.; Hu, Y.; Liu, L. L.; Wu, J. X.; Zhang, S. C.; Zhao, Q. C.; Ding, F.; Li, Q. W.; Zhang, J. Growth of close-packed semiconducting single-walled carbon nanotube arrays using oxygen-deficient TiO_2 nanoparticles as catalysts. *Nano Lett.* **2015**, *15*, 403–409.

[59] Zhang, L. L.; Sun, D. M.; Hou, P. X.; Liu, C.; Liu, T. Y.; Wen, J. F.; Tang, N. J.; Luan, J.; Shi, C.; Li, J. C. et al. Selective growth of metal-free metallic and semiconducting single-wall carbon nanotubes. *Adv. Mater.* **2017**, *29*, 1605719.

[60] Zhang, F.; Hou, P. X.; Liu, C.; Wang, B. W.; Jiang, H.; Chen, M. L.; Sun, D. M.; Li, J. C.; Cong, H. T.; Kauppinen, E. I. et al. Correction: Corrigendum: Growth of semiconducting single-wall carbon nanotubes with a narrow band-gap distribution. *Nat. Commun.* **2016**, *7*, 11563.

[61] Zhang, S. C.; Kang, L. X.; Wang, X.; Tong, L. M.; Yang, L. W.; Wang, Z. Q.; Qi, K.; Deng, S. B.; Li, Q. W.; Bai, X. D. et al. Arrays of horizontal carbon nanotubes of controlled chirality grown using designed catalysts. *Nature* **2017**, *543*, 234–238.

[62] Zhang, S. C.; Wang, X.; Yao, F. R.; He, M. S.; Lin, D. W.; Ma, H.; Sun, Y. Y.; Zhao, Q. C.; Liu, K. H.; Ding, F. et al. Controllable growth of $(n, n-1)$ family of semiconducting carbon nanotubes. *Chem* **2019**, *5*, 1182–1193.

[63] Zhu, Z. X.; Wei, N.; Cheng, W. J.; Shen, B. Y.; Sun, S. L.; Gao, J.; Wen, Q.; Zhang, R. F.; Xu, J.; Wang, Y. et al. Rate-selected growth

of ultrapure semiconducting carbon nanotube arrays. *Nat. Commun.* **2019**, *10*, 4467.

[64] Huang, S. M.; Qian, Y.; Chen, J. Y.; Cai, Q. R.; Wan, L.; Wang, S.; Hu, W. B. Identification of the structures of superlong oriented single-walled carbon nanotube arrays by electrodeposition of metal and Raman spectroscopy. *J. Am. Chem. Soc.* **2008**, *130*, 11860–11861.

[65] Chang, N. K.; Hsu, J. H.; Su, C. C.; Chang, S. H. Horizontally oriented carbon nanotubes coated with nanocrystalline carbon. *Thin Solid Films* **2009**, *517*, 1917–1921.

[66] Chu, H. B.; Cui, R. L.; Wang, J. Y.; Yang, J.; Li, Y. Visualization of individual single-walled carbon nanotubes under an optical microscope as a result of decoration with gold nanoparticles. *Carbon* **2011**, *49*, 1182–1188.

[67] Wang, J. T.; Li, T. Y.; Xia, B. Y.; Jin, X.; Wei, H. M.; Wu, W. Y.; Wei, Y.; Wang, J. P.; Liu, P.; Zhang, L. N. et al. Vapor-condensation-assisted optical microscopy for ultralong carbon nanotubes and other nanostructures. *Nano Lett.* **2014**, *14*, 3527–3533.

[68] Liu, K. H.; Hong, X. P.; Zhou, Q.; Jin, C. H.; Li, J. H.; Zhou, W. W.; Liu, J.; Wang, E. G.; Zettl, A.; Wang, F. High-throughput optical imaging and spectroscopy of individual carbon nanotubes in devices. *Nat. Nanotechnol.* **2013**, *8*, 917–922.

[69] Jorio, A.; Saito, R.; Hafner, J. H.; Lieber, C. M.; Hunter, M.; McClure, T.; Dresselhaus, G.; Dresselhaus, M. S. Structural (*n, m*) determination of isolated single-wall carbon nanotubes by resonant Raman scattering. *Phys. Rev. Lett.* **2001**, *86*, 1118–1121.

[70] Sfeir, M. Y.; Wang, F.; Huang, L. M.; Chuang, C. C.; Hone, J.; O'Brien, S. P.; Heinz, T. F.; Brus, L. E. Probing electronic transitions in individual carbon nanotubes by Rayleigh scattering. *Science* **2004**, *306*, 1540–1543.

[71] Wu, W. Y.; Yue, J. Y.; Lin, X. Y.; Li, D. Q.; Zhu, F. Q.; Yin, X.; Zhu, J.; Wang, J. T.; Zhang, J.; Chen, Y. et al. True-color real-time imaging and spectroscopy of carbon nanotubes on substrates using enhanced Rayleigh scattering. *Nano Res.* **2015**, *8*, 2721–2732.

[72] Bachilo, S. M.; Strano, M. S.; Kittrell, C.; Hauge, R. H.; Smalley, R. E.; Weisman, R. B. Structure-assigned optical spectra of single-walled carbon nanotubes. *Science* **2002**, *298*, 2361–2366.

[73] Deng, S. B.; Tang, J. Y.; Kang, L. X.; Hu, Y.; Yao, F. R.; Zhao, Q. C.; Zhang, S. C.; Liu, K. H.; Zhang, J. High-throughput determination of statistical structure information for horizontal carbon nanotube arrays by optical imaging. *Adv. Mater.* **2016**, *28*, 2018–2023.

[74] Jinkins, K. R.; Foradori, S. M.; Saraswat, V.; Jacobberger, R. M.; Dwyer, J. H.; Gopalan, P.; Berson, A.; Arnold, M. S. Aligned 2D carbon nanotube liquid crystals for wafer-scale electronics. *Sci. Adv.* **2021**, *7*, eabh0640.

[75] Joo, Y.; Brady, G. J.; Arnold, M. S.; Gopalan, P. Dose-controlled, floating evaporative self-assembly, and alignment of semiconducting carbon nanotubes from organic solvents. *Langmuir* **2014**, *30*, 3460–3466.

[76] Liu, L. J.; Han, J.; Xu, L.; Zhou, J. S.; Zhao, C. Y.; Ding, S. J.; Shi, H. W.; Xiao, M. M.; Ding, L.; Ma, Z. et al. Aligned, high-density semiconducting carbon nanotube arrays for high-performance electronics. *Science* **2020**, *368*, 850–856.

[77] Odom, T. W.; Huang, J. L.; Kim, P.; Lieber, C. M. Atomic structure and electronic properties of single-walled carbon nanotubes. *Nature* **1998**, *391*, 62–64.

[78] Sato, Y.; Yanagi, K.; Miyata, Y.; Suenaga, K.; Kataura, H.; Iijima, S. Chiral-angle distribution for separated single-walled carbon nanotubes. *Nano Lett.* **2008**, *8*, 3151–3154.

[79] Li, J.; He, Y. J.; Han, Y. M.; Liu, K.; Wang, J. P.; Li, Q. Q.; Fan, S. S.; Jiang, K. L. Direct identification of metallic and semiconducting single-walled carbon nanotubes in scanning electron microscopy. *Nano Lett.* **2012**, *12*, 4095–4101.

[80] Franklin, A. D. Nanomaterials in transistors: From high-performance to thin-film applications. *Science* **2015**, *349*.

[81] De Volder, M. F. L.; Tawfick, S. H.; Baughman, R. H.; Hart, A. J. Carbon nanotubes: Present and future commercial applications. *Science* **2013**, *339*, 535–539.

[82] Tans, S. J.; Verschueren, A. R. M.; Dekker, C. Room-temperature transistor based on a single carbon nanotube. *Nature* **1998**, *393*, 49–52.

[83] Martel, R.; Schmidt, T.; Shea, H. R.; Hertel, T.; Avouris, P. Single- and multi-wall carbon nanotube field-effect transistors. *Appl. Phys. Lett.* **1998**, *73*, 2447–2449.

[84] Javey, A.; Guo, J.; Wang, Q.; Lundstrom, M.; Dai, H. J. Ballistic carbon nanotube field-effect transistors. *Nature* **2003**, *424*, 654–657.

[85] Zhang, Z. Y.; Liang, X. L.; Wang, S.; Yao, K.; Hu, Y. F.; Zhu, Y. Z.; Chen, Q.; Zhou, W. W.; Li, Y.; Yao, Y. G. et al. Doping-free fabrication of carbon nanotube based ballistic CMOS devices and circuits. *Nano Lett.* **2007**, *7*, 3603–3607.

[86] Holmes, D. S.; DeBenedictis, E. P. Superconductor electronics and the international roadmap for devices and systems. In *2017 16th International Superconductive Electronics Conference* (*ISEC*), Naples, Italy, 2017.

[87] Liu, L. J.; Qiu, C. G.; Zhong, D. L.; Si, J.; Zhang, Z. Y.; Peng, L. M. Scaling down contact length in complementary carbon nanotube field-effect transistors. *Nanoscale* **2017**, *9*, 9615–9621.

[88] Javey, A.; Kim, H.; Brink, M.; Wang, Q.; Ural, A.; Guo, J.; McIntyre, P.; McEuen, P.; Lundstrom, M.; Dai, H. J. High-κ dielectrics for advanced carbon-nanotube transistors and logic gates. *Nat. Mater.* **2002**, *1*, 241–246.

[89] Javey, A.; Guo, J.; Farmer, D. B.; Wang, Q.; Wang, D. W.; Gordon, R. G.; Lundstrom, M.; Dai, H. J. Carbon nanotube field-effect transistors with integrated ohmic contacts and high-κ gate dielectrics. *Nano Lett.* **2004**, *4*, 447–450.

[90] Franklin, A. D.; Bojarczuk, N. A.; Copel, M. Consistently low subthreshold swing in carbon nanotube transistors using lanthanum oxide. *Appl. Phys. Lett.* **2013**, *102*, 013108.

[91] Franklin, A. D.; Luisier, M.; Han, S. J.; Tulevski, G.; Breslin, C. M.; Gignac, L.; Lundstrom, M. S.; Haensch, W. Sub-10 nm carbon nanotube transistor. *Nano Lett.* **2012**, *12*, 758–762.

[92] Franklin, A. D.; Tulevski, G. S.; Han, S. J.; Shahrjerdi, D.; Cao, Q.; Chen, H. Y.; Wong, H. S. P.; Haensch, W. Variability in carbon nanotube transistors: Improving device-to-device consistency. *ACS Nano* **2012**, *6*, 1109–1115.

[93] Franklin, A. D.; Koswatta, S. O.; Farmer, D. B.; Smith, J. T.; Gignac, L.; Breslin, C. M.; Han, S. J.; Tulevski, G. S.; Miyazoe, H.; Haensch, W. et al. Carbon nanotube complementary wrap-gate transistors. *Nano Lett.* **2013**, *13*, 2490–2495.

[94] Shulaker, M. M.; Hills, G.; Patil, N.; Wei, H.; Chen, H. Y.; Philip Wong, H. S.; Mitra, S. Carbon nanotube computer. *Nature* **2013**, *501*, 526–530.

[95] Franklin, A. D.; Chen, Z. H. Length scaling of carbon nanotube transistors. *Nat. Nanotechnol.* **2010**, *5*, 858–862.

[96] Qiu, C. G.; Zhang, Z. Y.; Xiao, M. M.; Yang, Y. J.; Zhong, D. L.; Peng, L. M. Scaling carbon nanotube complementary transistors to 5-nm gate lengths. *Science* **2017**, *355*, 271–276.

[97] Shulaker, M. M.; Wu, T. F.; Pal, A.; Zhao, L.; Nishi, Y.; Saraswat, K.; Wong, H. S. P.; Mitra, S. Monolithic 3D integration of logic and memory: Carbon nanotube FETs, resistive RAM, and silicon FETs. In *2014 IEEE International Electron Devices Meeting*, San Francisco, CA, USA, 2014.

[98] Shulaker, M. M.; Hills, G.; Park, R. S.; Howe, R. T.; Saraswat, K.; Wong, H. S. P.; Mitra, S. Three-dimensional integration of nanotechnologies for computing and data storage on a single chip. *Nature* **2017**, *547*, 74–78.

[99] Zhu, M. G.; Xiao, H. S.; Yan, G. P.; Sun, P. K.; Jiang, J. H.; Cui, Z.; Zhao, J. W.; Zhang, Z. Y.; Peng, L. M. Radiation-hardened and repairable integrated circuits based on carbon nanotube transistors with ion gel gates. *Nat. Electron.* **2020**, *3*, 622–629.

[100] Vandersypen, L.; Van Leeuwenhoek, A. Quantum computing—The next challenge in circuit and system design. in *2017 IEEE International Solid-State Circuits Conference* (*ISSCC*), San Francisco, CA, USA, 2017, pp 24–26.

[101] Xie, Y. N.; Zhong, D. L.; Fan, C. W.; Deng, X. S.; Peng, L. M.; Zhang, Z. Y. Highly temperature-stable carbon nanotube transistors and gigahertz integrated circuits for cryogenic electronics. *Adv. Electron. Mater.* **2021**, *7*, 2100202.

[102] Kim, S. H.; Haines, C. S.; Li, N.; Kim, K. J.; Mun, T. J.; Choi, C.; Di, J. T.; Oh, Y. J.; Oviedo, J. P.; Bykova, J. et al. Harvesting electrical energy from carbon nanotube yarn twist. *Science* **2017**, *357*, 773–778.

[103] Brady, G. J.; Way, A. J.; Safron, N. S.; Evensen, H. T.; Gopalan, P.; Arnold, M. S. Quasi-ballistic carbon nanotube array transistors with current density exceeding Si and GaAs. *Sci. Adv.* **2016**, *2*, e1601240.

[104] He, X. W.; Gao, W. L.; Xie, L. J.; Li, B.; Zhang, Q.; Lei, S. D.; Robinson, J. M.; Hároz, E. H.; Doorn, S. K.; Wang, W. P. et al. Wafer-scale monodomain films of spontaneously aligned single-walled carbon nanotubes. *Nat. Nanotechnol.* **2016**, *11*, 633–638.

[105] Si, J.; Zhong, D. L.; Xu, H. T.; Xiao, M. M.; Yu, C. X.; Zhang, Z. Y.; Peng, L. M. Scalable preparation of high-density semiconducting carbon nanotube arrays for high-performance field-effect transistors. *ACS Nano* **2018**, *12*, 627–634.

[106] Sun, W.; Shen, J.; Zhao, Z.; Arellano, N.; Rettner, C.; Tang, J. S.; Cao, T. Y.; Zhou, Z. Y.; Ta, T.; Streit, J. K. et al. Precise pitch-scaling of carbon nanotube arrays within three-dimensional DNA nanotrenches. *Science* **2020**, *368*, 874–877.

[107] Cheng, Z. H.; Pang, C. S.; Wang, P. Q.; Le, S. T.; Wu, Y. Q.; Shahrjerdi, D.; Radu, I.; Lemme, M. C.; Peng, L. M.; Duan, X. F. et al. How to report and benchmark emerging field-effect transistors. *Nat. Electron.* **2022**, *5*, 416–423.